

## Variations in Hawaiian Plume Flux Controlled by Ancient Mantle Depletion

Paul Béguelin<sup>1,2</sup> , Andreas Stracke<sup>1</sup> , Maxim D. Ballmer<sup>3</sup> , Shichun Huang<sup>4</sup> ,  
Michael Willig<sup>1,5</sup>, and Michael Bizimis<sup>6</sup> 

<sup>1</sup>Institut für Mineralogie, Universität Münster, Münster, Germany, <sup>2</sup>Now at School of Earth and Environmental Sciences, Cardiff University, Cardiff, UK, <sup>3</sup>Department of Earth Sciences, University College London, London, UK, <sup>4</sup>Department of Earth, Environmental, and Planetary Sciences, University of Tennessee, Knoxville, TN, USA, <sup>5</sup>Now at GS1 Netherlands, Amstelveen, The Netherlands, <sup>6</sup>School of Earth, Ocean and the Environment, University of South Carolina, Columbia, SC, USA

**Peer Review** The peer review history for this article is available as a PDF in the Supporting Information.

### Key Points:

- We present new Ce isotope data for Hawaii lavas and use a physical-chemical model to constrain plume composition from multi-isotope data
- The Hawaiian mantle source is >94% peridotite which has been variably melt-depleted before being entrained into the Hawaiian plume
- Upwelling of buoyant depleted peridotite caused increases in plume volume flux that coincided with a spike in magmatism 1–3 Myr ago

### Supporting Information:

Supporting Information may be found in the online version of this article.

### Correspondence to:

P. Béguelin,  
BéguelinP@cardiff.ac.uk

### Citation:

Béguelin, P., Stracke, A., Ballmer, M. D., Huang, S., Willig, M., & Bizimis, M. (2025). Variations in Hawaiian plume flux controlled by ancient mantle depletion. *AGU Advances*, 6, e2024AV001434. <https://doi.org/10.1029/2024AV001434>

Received 26 JUL 2024

Accepted 4 FEB 2025

### Author Contributions:

**Conceptualization:** Paul Béguelin, Andreas Stracke, Michael Bizimis

**Data curation:** Paul Béguelin

**Formal analysis:** Paul Béguelin

**Funding acquisition:** Paul Béguelin, Andreas Stracke, Michael Bizimis

**Investigation:** Paul Béguelin, Michael Willig

**Methodology:** Paul Béguelin, Andreas Stracke, Maxim D. Ballmer, Michael Willig

**Project administration:** Paul Béguelin, Andreas Stracke, Michael Bizimis

© 2025. The Author(s).

This is an open access article under the terms of the [Creative Commons Attribution License](https://creativecommons.org/licenses/by/4.0/), which permits use, distribution and reproduction in any medium, provided the original work is properly cited.

**Abstract** Mantle plumes—upwellings of buoyant rock in Earth's mantle—feed hotspot volcanoes such as Hawai'i. The size of volcanoes along the Hawai'i–Emperor chain, and thus the magma flux of the Hawaiian plume, has varied over the past 85 million years. Fifteen and two million years ago, rapid bursts in magmatic production led to the emergence of large islands such as Pūhāhonu, Maui Nui and Hawai'i, but the underlying mechanisms remain enigmatic. Here, we use new radiogenic Ce–Sr–Nd–Hf isotope data of Hawaiian shield lavas to quantify the composition and proportion of the different constituents of the Hawaiian plume over time. We find that most of the Hawaiian mantle source is peridotite that has experienced variable degrees of melt depletion before being incorporated into the plume. We show that the most isotopically enriched LOA-type compositions arise from the aggregation of melts from more depleted, trace element-starved peridotite, causing the over-visibility of melts from recycled crust in the mixture. Our results also show that upwelling of chemically more depleted, and thus less dense, more buoyant mantle peridotite occurred synchronously to an observed burst of magma production. Buoyancy variations induced by variably depleted peridotite may not only control the temporal patterns of volcanic productivity in Hawai'i, but also those of other plumes world-wide. The excess buoyancy of depleted peridotite may therefore be an underrated driving force for convective mantle flow, trigger and sustain active upwelling of relatively cool plumes, and control the geometry of mantle upwellings from variable depths.

**Plain Language Summary** Isolated, intra-plate volcanic centers such as Hawai'i are generated by plumes ascending from Earth's deep interior. The Hawaiian plume is long-lived (>85 million years) and, over time, has formed a chain of volcanoes atop the drifting Pacific tectonic plate. Geophysical observations have revealed that the volume of magma coming out of the plume sharply increased about 15 and <3 million years ago. The underlying cause of these bursts is unknown. The natural decay of mildly radioactive isotopes over millions to billions of years causes differences in the isotope ratios of strontium, cerium, neodymium, and hafnium which are useful for tracking the time-integrated chemical composition of the different plume materials. We present new isotope measurements for a representative set of Hawaiian lavas and build a numerical model that uses this multi-variate data set to calculate plume composition and density through time. We identify plume material that has a lower density due to ancient melting events which causes episodic plume flux increases in good agreement with geophysical observations. Compositional-driven buoyancy may thus be an underrated driving force for the convection of our planet's interior.

## 1. Introduction

### 1.1. Hawaiian Plume Upwelling and Volcanism

Mantle plumes were originally envisaged as long-lived, thermal upwellings from deep-mantle boundary layers (Morgan, 1971). Classical plume models predict that the impingement of a large plume head onto the lithosphere results in an initial burst of magma production, followed by reduced magmatic activity over a steady, columnar plume conduit (Campbell, 2007). A near steady plume flux between 85 and 20 Ma, and constant magma production rates of ca.  $2 \pm 1 \text{ m}^3 \text{ s}^{-1}$  characterize the Hawaiian plume activity along the Hawai'i–Emperor seamount chain (Van Ark & Lin, 2004; Vidal & Bonneville, 2004; Wessel, 2016) (Figure 1). At ~15 and <3 Ma, however, volcanic activity peaked ( $8 \pm 2 \text{ m}^3 \text{ s}^{-1}$ ), and rapidly built up the large Pūhāhonu (Gardner) volcano and the

**Resources:** Andreas Stracke, Shichun Huang, Michael Bizimis  
**Software:** Paul Béguelin  
**Supervision:** Andreas Stracke, Michael Bizimis  
**Visualization:** Paul Béguelin  
**Writing – original draft:** Paul Béguelin  
**Writing – review & editing:** Paul Béguelin, Andreas Stracke, Maxim D. Ballmer, Shichun Huang, Michael Willig, Michael Bizimis

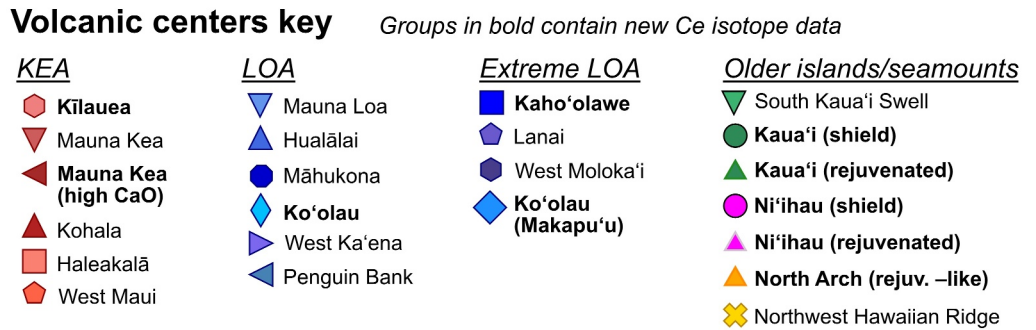
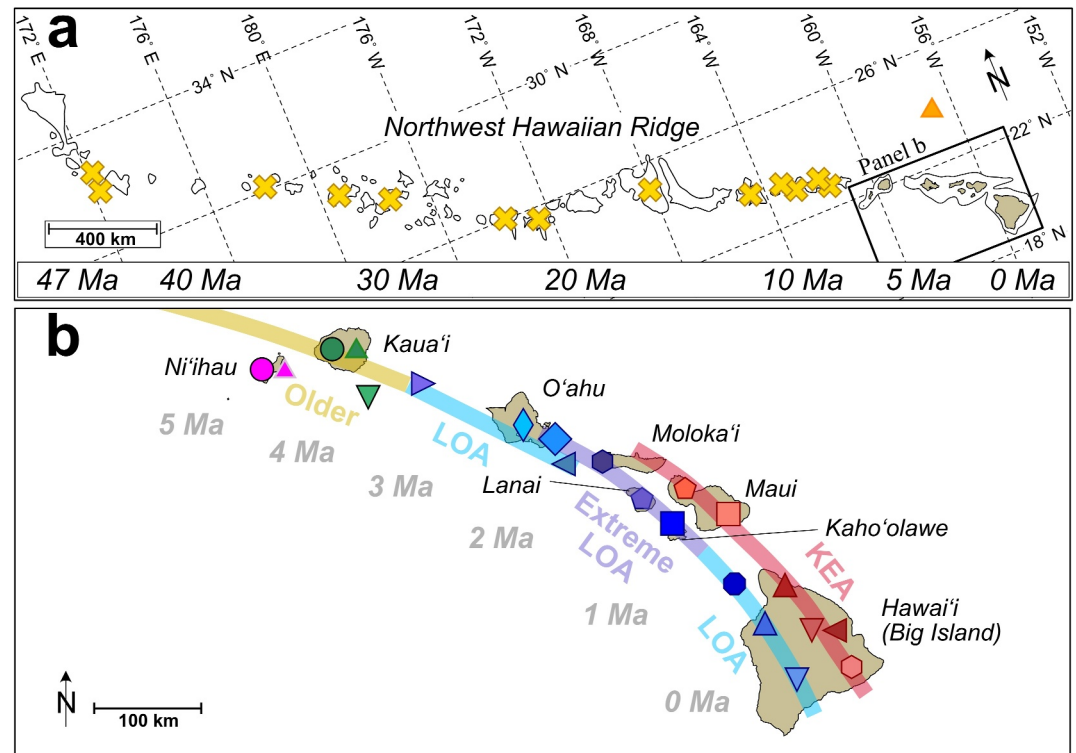


**Figure 1.** Maps of (a) the Hawaiian hotspot track and (b) the Hawaiian Islands. Panel a shows seamounts produced by the Hawaiian plume between 50 Ma and present-day. Outlines correspond to a bathymetry of  $-2,000$  m. Time scale at the bottom represents seamounts ages. Panel b shows the Hawaiian Islands (younger than 6 Ma) with the *Older*, *KEA*, *LOA*, and *Extreme LOA* lineaments discussed in the text. Symbols in panels a and b denote the location of the volcanic centers discussed in this study. For names and details of Northwest Hawaiian Ridge localities, see Harrison et al. (2017). For detailed location data of the rest of the samples, see references listed in Table S2 in Supporting Information S2.

Hawaiian Islands. These temporal variations in Hawaiian plume flux remain difficult to explain, even with a modern view of mantle plumes as transient, thermochemical upwellings with complex shapes and flow patterns (Davaille et al., 2018; Farnetani & Samuel, 2005; Kumagai et al., 2008; Ribe et al., 2007).

According to Stokes' Law, plume flux, and thus magma production, varies linearly with its density deficit, or excess buoyancy, relative to the ambient mantle (assuming a constant plume radius: d'Acremont et al., 2003; Le Bars & Davaille, 2004). In the classic plume model of Morgan (1971), this density deficit is purely thermal and scales with the thermal expansion of peridotite, the major constituent of Earth's mantle (Ringwood, 1969; Stracke, 2012). For 100 K excess potential temperature, peridotite density decreases by  $\sim 10 \text{ kg m}^{-3}$  (Griffiths & Campbell, 1990). But mantle plumes may not only be hotter, they may also be compositionally distinct from their surroundings (e.g., Béguelin et al., 2017; Chauvel et al., 2008; DeFelice et al., 2019; Hofmann, 1997; Salters et al., 2006; Sanfilippo et al., 2024; Stracke & Béguelin, 2024; Stracke et al., 2003, 2019).

Incorporation of recycled crust (oceanic crust (OC)  $\pm$  sediments) within a mostly peridotitic plume, for example, may influence plume composition, increasing its density by  $+0.6$  to  $+1.8 \text{ kg m}^{-3}$  per percent of recycled crust (Ishii et al., 2019; Ricolleau et al., 2010). Even though recycled crust typically constitutes  $<10\%$  of mantle plumes (Stracke, 2012; Shorttle et al., 2014; Lambart et al., 2016; Stracke & Béguelin, 2024; Stracke et al., 2022, but see Sobolev et al., 2007 for different estimates), considerable excess temperature is required for plumes to be able to carry such excess density (Bao et al., 2022). The excess temperatures of mantle plumes estimated from petrology (Herzberg & Gazel, 2009; Putirka, 2008) or seismic velocities (Bao et al., 2022), however, are not always sufficiently high to offset the negative buoyancy of relatively large amounts of dense recycled crust. Therefore, additional buoyancy sources are required to promote active upwelling of comparatively cool plumes, which are still hotter than the ambient mantle (Bao et al., 2022). The elusive source of buoyancy may arise from peridotite that has previously been melted, which is thought to be present in the Hawaiian plume (Béguelin et al., 2019; Bizimis et al., 2005, 2007; DeFelice et al., 2019; Frey et al., 2005; Harrison et al., 2020; Salters et al., 2006; Stracke et al., 1999, 2019). Partial melting reduces peridotite density by ca.  $10 \text{ kg m}^{-3}$  for 6% of melt extraction (Afonso & Schutt, 2012), similar to the effect of thermal expansion for a 100 K hotter mantle. Variably depleted and light peridotite in plumes may therefore critically contribute to their overall density deficit (Sanfilippo et al., 2024; Shorttle et al., 2014; Stracke & Béguelin, 2024; Stracke et al., 2019).

However, the extent of peridotite depletion and its role in plume upwelling and magmatism remains poorly understood. Importantly, the terms enriched versus depleted should not be confused or equated to fertile versus refractory. Peridotites are quantitatively *depleted* in incompatible trace elements after 2%–5% melting, whereas it takes 17%–20% melting to make them *refractory*, that is, to become clinopyroxene-poor harzburgites that require several 100 K temperature excess to melt in the shallow mantle. In other words, not all depleted peridotites are refractory, but all refractory peridotites are depleted. Peridotites with 5%–17% melt-depletion, for example, are highly incompatible element depleted, but remain clinopyroxene-rich peridotites (Iherzolites), and therefore have high enough Al-Ca contents to produce abundant melts at ambient mantle temperatures (Byerly & Lassiter, 2014; Sani et al., 2020; Walter & Cottrell, 2025). This is because Al and Ca are less incompatible than Sr, Nd, Hf, Pb. As such, prior melting events can significantly decrease the Sr, Nd, Hf, Pb abundances, but still leave reasonably high Al-Ca contents as clinopyroxene.

Although the excess temperature of the Hawaiian plume (Bao et al., 2022; Green & Falloon, 2005; Herzberg & Gazel, 2009; Putirka, 2005, 2008) has sustained active upwelling for  $>85$  Ma, additional factors are required to explain the observed increases in magma flux of the Hawaiian plume at  $\sim 15$  and  $<3$  Ma (Van Ark & Lin, 2004; Vidal & Bonneville, 2004; Wessel, 2016). Critically, periods of accelerated magma production correlate with changes in the Pb isotope ratios of Hawaiian lavas (higher  $^{208}\text{Pb}^*/^{206}\text{Pb}^*$ , Harrison et al., 2017: their Figure 3). Here, we investigate whether changes in Hawaiian plume composition, and specifically, variations in the relative abundance and composition of peridotite and recycled crust, may intermittently decrease plume density, hence increase plume buoyancy, and cause the observed pulses of high magma production.

## 1.2. Ce-Nd-Hf Isotope Constraints on Hawaiian Plume Composition

Combined Ce-Nd-Hf isotope ratios are a unique tool for evaluating peridotite abundance and composition in melts from a heterogeneous mantle that consists of peridotite and recycled crust (see detailed quantitative discussion in Willig et al., 2020). Incompatible element depleted peridotites have much lower Ce/(Nd, Hf) than recycled oceanic or continental crust. Therefore, mixing lines between melts from incompatible element depleted peridotite and recycled crust in  $\epsilon_{\text{Ce}}-\epsilon_{\text{Nd}}$  and  $\epsilon_{\text{Ce}}-\epsilon_{\text{Hf}}$  diagrams are highly curved and at a high angle to mixing lines between melts from recycled OC and sediments (Willig et al., 2020) (Figures 2a and 2b). A similar, but more muted effect is observed in  $\epsilon_{\text{Hf}}-\epsilon_{\text{Nd}}$  diagrams (Salters et al., 2011) (Figure 2c, Figure S1 in Supporting Information S1). Hence, mixing melts from variably depleted peridotites in constant proportion to melts from recycled OC, and with different proportions of melts from recycled sediments, results in an array of vertically stacked mixing trends in  $\epsilon_{\text{Ce}}-\epsilon_{\text{Hf}}$  space that are subparallel to the global trends of oceanic basalts (Figures 2b and 3). Such vertically stacked trends (Figures 2b, 2d, and 3) are a clear indication that the mantle sources of oceanic basalts contain variably incompatible element depleted peridotites (Willig et al., 2020).

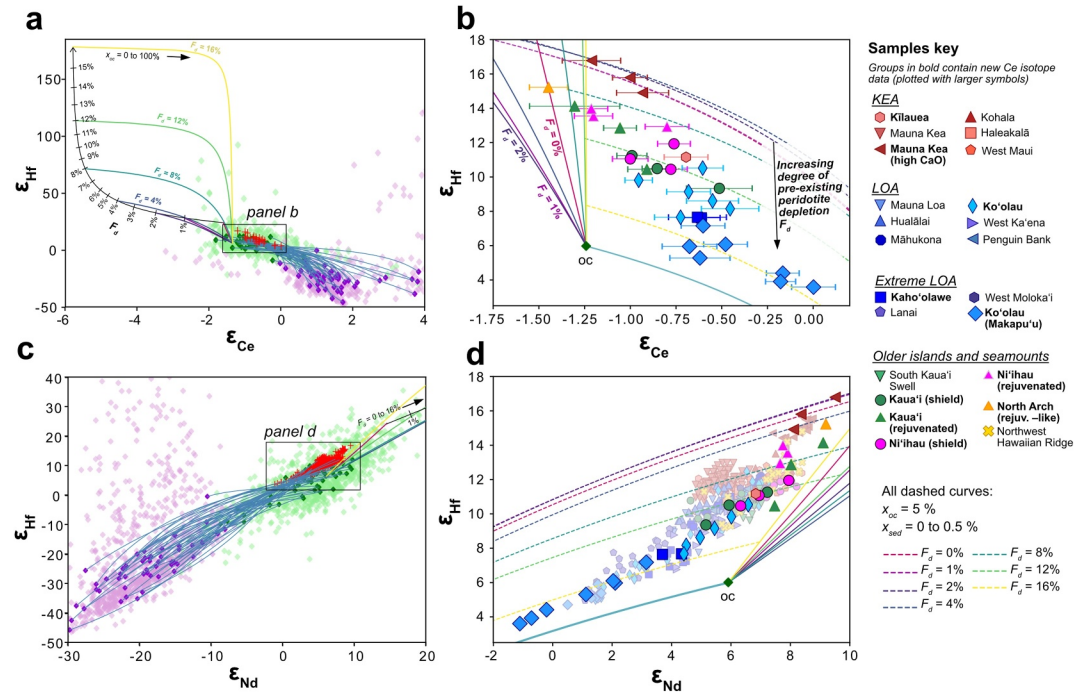


**Figure 2.** The diagrams show the  $\epsilon_{Ce}-\epsilon_{Hf}$  (a), (b) and  $\epsilon_{Nd}-\epsilon_{Hf}$  systematics (c), (d) of the Hawaiian samples reported in this study. The  $\epsilon_{Ce}$ ,  $\epsilon_{Nd}$ ,  $\epsilon_{Hf}$  notations express isotope ratios as 1/10,000 deviations from  $^{138}\text{Ce}/^{136}\text{Ce} = 1.336897$ ,  $^{143}\text{Nd}/^{144}\text{Nd} = 0.512630$ ,  $^{176}\text{Hf}/^{177}\text{Hf} = 0.282785$  (CHUR values from Bouvier et al., 2008; Willig & Stracke, 2019).  $\epsilon_{Ce}$  error bars in (b) represent 2 S.E. uncertainties on each side. Uncertainties of Nd-Hf isotope ratios are smaller than the symbols. Colored symbols in (b), (d) are the data for Hawaiian samples reported in this study and correspond to the red crosses in panels (a), (c). Smaller, light colored symbols in panel (d) are literature data of Hawaiian samples (see Table S2 in Supporting Information S2 for references). Light purple and green diamond symbols in panels (a), (c) are 1,000 representative compositions of recycled sediment (purple) and recycled oceanic crust (OC) (green) calculated with our *Monte Carlo* model. The solid purple and green diamond symbols represent the 50 solutions that best reproduce the isotopic variability of the Hawaiian lavas. Solid pink-blue-green-yellow lines in panels (a), (c) are mixing curves between recycled OC (oc, green diamonds) and variably depleted peridotite (different  $F_d$  values, black curve in panel (a)), which are also shown in the enlarged parts of the diagrams in panels (b), (d) (see color key for corresponding  $F_d$  values in panel (d)). Solid purple lines in panels (a), (c) are mixing lines between recycled OC and marine sediments (purple diamonds), hence indicate locations of bulk recycled crust (OC + different amounts of sediments, shown for the 50 best solutions). Dashed curves in panels (b), (d) represent varying amounts of sediments (0%–0.5%) added to mixtures between melts from variable peridotites and oc in constant proportion in the plume source ( $x_{oc} = 5\%$ ). Note that each of these dashed lines is for a peridotite component with different extent of incompatible element depletion (corresponding to different  $F_d$  values, (a)). These vertically stacked trends are subparallel to the trends of lavas from a given Hawaiian locality and are a decisive indication that the Hawaiian plume contains variably incompatible element depleted peridotite (Willig et al., 2020). Additional clarifications of this effect are given in Figure 3, and additional plots can be found in Figure S1 in Supporting Information S1.

## 2. Methods

### 2.1. Sample Selection

Hawaiian volcanoes go through a characteristic time sequence of volcanic activity (Clague & Dalrymple, 1987; Clague & Sherrod, 2014). The most voluminous stage of Hawaiian volcanism is the tholeiitic shield stage, followed by the post-shield stage with eruption of more differentiated lavas. After a ca. 0.6–2 Myr gap in activity, a volumetrically minor, post-erosional stage of volcanic activity, also known as the rejuvenated stage, occurs at some, but not all volcanoes, erupting highly alkaline lavas (Clague & Frey, 1982; Garcia et al., 2010).

We analyzed a selection of samples from several Hawaiian volcanoes for Ce isotopes, covering the entire published Sr–Nd–Hf–Pb isotope range for Hawaii. We present Ce isotope ratios for shield stage lavas from Kilauea ( $n = 1$ ), Mauna Kea ( $n = 3$ , high CaO lavas: DeFelice et al., 2019), Kaho'olawe ( $n = 2$ , Huang et al., 2005), Ko'olau volcano on the island of O'ahu ( $n = 6$ , from the KSDP drill core, main-shield stage: Haskins & Garcia, 2004; Huang & Frey, 2005; Fekiacova et al., 2007) and 8 samples from its late-shield Makapu'u stage: Salters

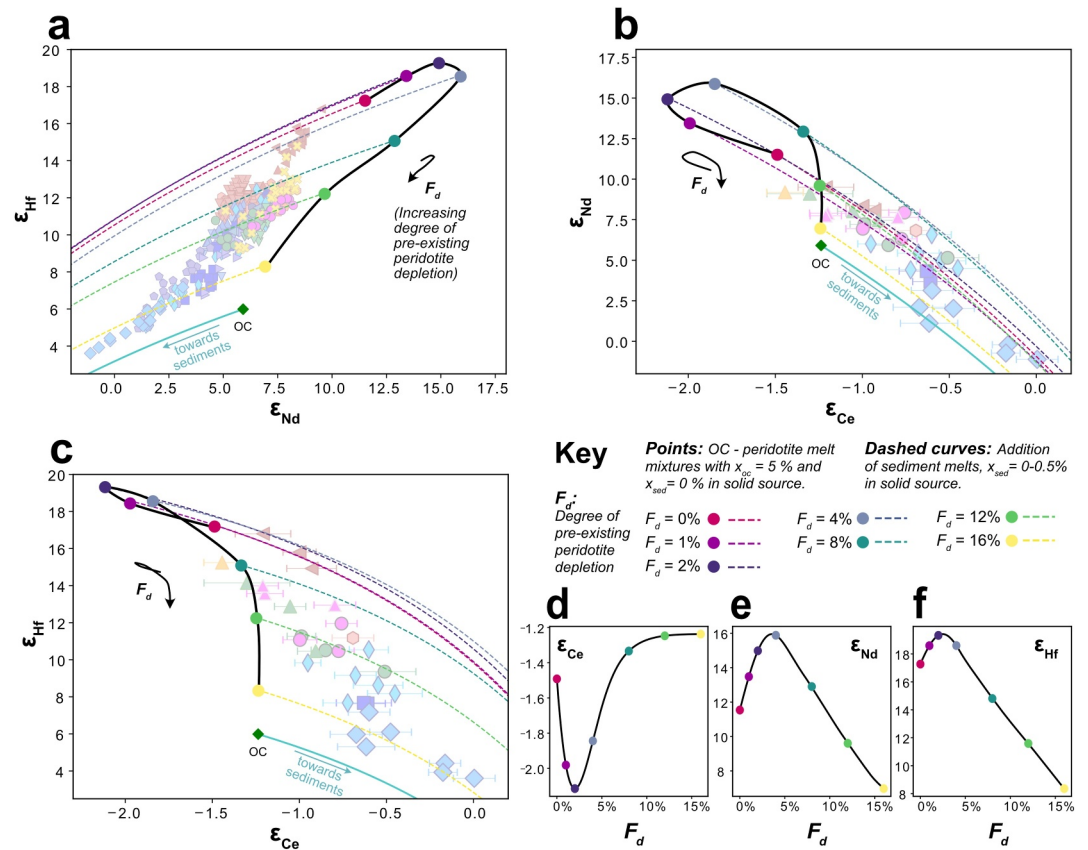


**Figure 3.** The diagrams illustrate the link between radiogenic isotope systematics and peridotite depletion. The solid, colored circles along the thick black curves in panels (a), (b), and (c) represent the isotope composition of aggregated melts from a solid source with 5% of oceanic crust (OC) ( $x_{oc} = 5\%$ ) and a 1.5 Ga peridotite with varying extents of melt depletion ( $F_d = 0-16\%$ , see key). Dashed curves are as in Figure 2, representing varying amounts of sediments (0%–0.5%), added to the mixture of melts from peridotite and recycled OC. Background data and OC – sediments curves are as in Figure 2 (see samples key therein). Panels (d), (e), and (f) show the isotope signatures of aggregate melts from OC and peridotite with variable extent of prior depletion  $F_d$ . See Stracke and Béguelin (2024) for a detailed discussion of this effect, and Figure S1 in Supporting Information S1 for plots including Sr isotope ratios.

et al. (2011) (Table S1 in Supporting Information S2). We also report Ce isotope data for the shield and rejuvenated stages of Kaua'i and Ni'ihau islands (3 samples per stage and per island), and for the rejuvenated-like North Arch Volcanic Field ( $n = 1$ ), previously described for major, trace elements and other radiogenic isotopes (Béguelin et al., 2019; Cousens & Clague, 2015; Dixon et al., 2008; Frey et al., 2000). The location of volcanic centers is shown in Figure 1, and references and existing data can be found in Tables S1 and S2 in Supporting Information S2.

In addition to the samples measured for Ce isotopes, we used a literature data set for Sr–Nd–Hf isotope-based geochemical modeling. This data set is a compilation of 530 shield stage samples from the GEOROC database (Sarbas, 2008) downloaded on 19 November 2021 and filtered for duplicates (Table S2 in Supporting Information S2 and references therein). Literature on Hawaiian basalts sub-divide shield lavas based on the locus of eruption along and across the chain and based on their isotope systematics. The presence of two parallel chains of volcanic centers between Oahu and Hawai'i Big Island yield a *KEA* (eastern) and a *LOA* (western) group (Abouchami et al., 2005; Huang et al., 2011; Jackson et al., 1975; Tatsumoto, 1978; Weis et al., 2011, 2020) (Figure 1b). Older shield lavas can be grouped into an *Older islands and seamounts* group (Béguelin et al., 2019). The *LOA* group is often subdivided into a *LOA* and an *Extreme LOA* group, based on the particularly low Nd–Hf isotope and high Sr isotope ratios of lavas at mid-length of the *LOA* chain (e.g., Weis et al., 2020) (Figure 1b). We group all shield lavas discussed into these four groups, as detailed in the keys of Figures 1 and 2.

## 2.2. Analytical Details

For Ce isotope measurements, 60–600 mg of rock powder (depending on Ce concentration, to yield a minimum of 6  $\mu\text{g}$  Ce) was dissolved in a 3:1 concentrated HF:HNO<sub>3</sub> mixture at ca. 110°C. Samples were then redissolved in 1 N HNO<sub>3</sub>, centrifuged and loaded on ion exchange columns containing TRU resin (Eichrom, USA) (Pin et al., 1994). 1 N HNO<sub>3</sub> was used for matrix removal, and rare earth elements (REE) were collected in 1 N HCl. This part of the chemistry was carried out at the Center for Elemental Mass Spectrometry, University of South Carolina (USA) and at the Institut für Mineralogie, Universität Münster (Germany). REE aliquots were then dried down in concentrated HNO<sub>3</sub> and loaded on ion exchange columns containing Ln resin (Eichrom, USA). 10 N HNO<sub>3</sub> + 0.3% KBrO<sub>3</sub> was used to oxidize Ce<sup>3+</sup> to Ce<sup>4+</sup>, promoting retention of Ce<sup>4+</sup> on the column over the other (trivalent) REE (Tazoe, Obata, Amakawa, et al., 2007; Tazoe, Obata, & Gamo, 2007; Willig & Stracke, 2018). Cerium was then collected using 6N HCl + H<sub>2</sub>O<sub>2</sub>. This second half of the chemistry was carried out at Universität Münster for all samples.

Cerium isotope ratios were measured on a Thermo Scientific Triton thermal ionization mass spectrometer at the Universität Münster, following the method of Willig and Stracke (2018). 2–3  $\mu\text{g}$  of Ce was loaded on zone-refined Re filaments in HCl with 1  $\mu\text{l}$  of 1.5 M H<sub>3</sub>PO<sub>4</sub>. Cerium oxides were measured on faraday cups with a 10<sup>10</sup>  $\Omega$  amplifier for the most abundant <sup>140</sup>Ce<sup>16</sup>O, and 10<sup>11</sup>  $\Omega$  amplifiers for <sup>136</sup>Ce<sup>16</sup>O, <sup>138</sup>Ce<sup>16</sup>O, <sup>142</sup>Ce<sup>16</sup>O, <sup>142</sup>Ce<sup>18</sup>O. Contributions from the <sup>140</sup>Ce<sup>16</sup>O tail on <sup>136</sup>Ce<sup>16</sup>O and <sup>138</sup>Ce<sup>16</sup>O were accounted for by measuring the average 151.4/<sup>140</sup>Ce<sup>16</sup>O, 153.4/<sup>140</sup>Ce<sup>16</sup>O and 154.4/<sup>140</sup>Ce<sup>16</sup>O half-mass to oxide ratios for a given sample and subtracting the exponentially interpolated tail to the <sup>140</sup>Ce<sup>16</sup>O signal on each cycle (details of this tail correction are given in Willig & Stracke, 2018). <sup>136</sup>Ce/<sup>142</sup>Ce = 0.01688 was used to correct for instrumental mass fractionation using the exponential law. Each measurement consisted of ~60 cycles of 40 s integration for full-mass measurements and 6 s for half-mass measurements (−0.5 and +0.5 amu). Idle time after each magnet setting change was 3 s. Offline data reduction and further analytical details are given in Willig and Stracke (2018) and Willig et al. (2020).

Accuracy was monitored by repeated measurement of the Ames cerium standard (Ames Laboratory, USA) yielding an average <sup>138</sup>Ce/<sup>136</sup>Ce = 1.337355 with a reproducibility of 24 ppm (2 standard error,  $n = 17$ , over a 10-day period), and, in another multi-day session, <sup>138</sup>Ce/<sup>136</sup>Ce = 1.337340 with a reproducibility of 10 ppm (2 standard error,  $n = 8$ , over a 9-day period). Measured sample values are reported relative to <sup>138</sup>Ce/<sup>136</sup>Ce<sub>Ames</sub> = 1.337366, as in Willig and Stracke (2018). The typical internal precision for a single measurement was 13 ppm (2 standard error of all valid cycles; ratios outside of 2.5 standard error of the average value for a measurement were rejected). Samples with low Ce concentrations resulting in low intensity measurements with an internal precision >17 ppm were discarded unless no better replicate could be made, in which case two low intensity measurements were averaged (for samples U1, U9 and KM7). For these measurements, respective errors were propagated by taking the square root of the sum of squared errors, divided by 2.

Measured <sup>138</sup>Ce/<sup>136</sup>Ce ratios are converted to  $\epsilon_{\text{Ce}}$  with <sup>138</sup>Ce/<sup>136</sup>Ce<sub>CHUR</sub> = 1.336897 (CHUR = chondritic uniform reservoir) (Willig & Stracke, 2019). Similarly, the Nd–Hf isotope data are expressed as  $\epsilon_{\text{Nd}}$  and  $\epsilon_{\text{Hf}}$  using <sup>143</sup>Nd/<sup>144</sup>Nd<sub>CHUR</sub> = 0.512630 and <sup>176</sup>Hf/<sup>177</sup>Hf<sub>CHUR</sub> = 0.282785 (Bouvier et al., 2008). Results are presented in Table S1 in Supporting Information S2, and in Figure 2b.

## 3. Results

### 3.1. Isotope Data

Our new Ce–(Nd–Hf) isotope data for a representative selection of well-documented Hawaiian lavas ( $n = 32$ , Figures 1 and 2, Figure S1 in Supporting Information S1, Table S1 in Supporting Information S2) form an array of vertically stacked trends in Figure 2b, with variable  $\epsilon_{\text{Hf}}$  for near invariable  $\epsilon_{\text{Ce}}$ . The  $\epsilon_{\text{Ce}} - \epsilon_{\text{Nd}} - \epsilon_{\text{Hf}}$  systematics of the Hawaiian lavas therefore require that melts from different low  $\epsilon_{\text{Ce}}$  source components, that is, variably depleted peridotites with low time-integrated La/Ce, control their Ce–Nd–Hf isotope variability (Figures 2 and 3, discussion in Willig et al., 2020).

Among the shield lavas, the *Older islands and seamounts* group range from  $\epsilon_{\text{Ce}} = -1.0$  to  $-0.5$ , with lower values for *KEA* lavas ( $\epsilon_{\text{Ce}} = -1.2$  to  $-0.7$ ) and similar values for *LOA* lavas ( $\epsilon_{\text{Ce}} = -0.95$  to  $-0.45$ ). *Extreme LOA* lavas have higher values, ranging from  $\epsilon_{\text{Ce}} = -0.7$  to 0.0 (Figure 2 and Figure S1 in Supporting Information S1). These *Extreme LOA* values form distinct trends in Ce–Nd, Ce–Hf and Ce–Sr isotope diagrams (Figure 2, Figure S1 in Supporting Information S1).

In a mixing model where melts from increasingly depleted peridotite and melts from recycled crust mix, the *Extreme LOA* trend can readily be explained by the sampling of more depleted peridotite, as discussed in Salters et al. (2006) and shown in Figures 2b, 2d and 3a–3c. This counter-intuitive effect is caused by the very low Nd and Hf content in such peridotite compared to less depleted peridotite, and thus the Nd and Hf isotope ratios of aggregated melts approach those of the recycled crust (Figures 3d–3f, Figures S1d–S1g in Supporting Information S1). While the Sm/Nd and Lu/Hf ratios of peridotite increase with melt-depletion, leading to more radiogenic  $\epsilon_{Nd}$  and  $\epsilon_{Hf}$  values, Nd and Hf concentrations decrease exponentially, and become the primary factor controlling the isotope ratios of the aggregated melts from a mantle source consisting of heterogeneous peridotites and recycled crust. Melts from peridotites with comparatively higher trace element concentrations (<5% melt depletion) influence isotopically enriched melts from a given amount of recycled crust more than melts from a highly trace element depleted peridotite (>5% melt depletion), because the latter are almost devoid of Nd and Hf. See Figure 3 and Figure S1 in Supporting Information S1 for a detailed representation of this effect. See also Stracke and Béguelin (2024) for a detailed quantitative discussion.

The magnitude of this effect, however, depends on many other factors such as the isotope and elemental composition of recycled crust, the recycling and depletion ages, and the melting degrees of these components. We therefore build a quantitative model of Hawaiian plume source and magmatism to interpret these data with a full consideration of a large parameter space.

## 4. Discussion

### 4.1. Determining Hawaiian Plume Composition Using a Quantitative Model

Building on the chemical and isotopic composition of the erupted lavas, including the new Ce isotope constraint, we developed a simplified physical-chemical model of plume melting to constrain the relative abundance of variably depleted peridotite, recycled OC and sediments in the Hawaiian mantle plume (Blichert-Toft et al., 1999; Huang et al., 2005; Lassiter & Hauri, 1998; Salters et al., 2006), as well as plume potential temperature. For each sample, this model quantifies the plume constituents and temperature on the basis of isotopic signatures of each source component. The present-day isotopic signature of each component depends on its age and composition, and thus is randomly varied in a *Monte Carlo* approach. We use the samples with Ce isotope data to constrain the parameter space, that is, the isotopic composition of each plume component, as detailed in Figure 4, Section 4.1.1 below, and in the Text S1 in Supporting Information S1. Within the so-defined parameter space, we quantify the source abundance of the different plume components and plume potential temperature for 530 literature samples (see Figures 1 and 2) that do not have Ce isotope data.

An abbreviated description of the model calculations is given in the following section (Section 4.1.1), and further details are provided in the Text S1 in Supporting Information S1. All the modeling is performed in *Python 3.9*, using the packages *NumPy 1.21.5*, *Pandas 1.4.4* and *SciPy 1.9.1* (Harris et al., 2020; McKinney, 2010; Virtanen et al., 2020).

#### 4.1.1. Model Design

We calculate the isotope ratio of a modeled plume basalt by mass balance, assuming the basalt is a mixture of melts from three plume components: (a) peridotite (per), (b) recycled OC (oc), and (c) marine sediments (sed).

$$f_{\text{basalt}}^i \text{IR}_{\text{basalt}}^i = f_{\text{per}}^i \text{IR}_{\text{per}}^i + f_{\text{oc}}^i \text{IR}_{\text{oc}}^i + f_{\text{sed}}^i \text{IR}_{\text{sed}}^i \quad (1)$$

and thus 
$$\text{IR}_{\text{basalt}}^i = (f_{\text{per}}^i \text{IR}_{\text{per}}^i + f_{\text{oc}}^i \text{IR}_{\text{oc}}^i + f_{\text{sed}}^i \text{IR}_{\text{sed}}^i) / f_{\text{basalt}}^i$$

with 
$$f_{\text{basalt}}^i = f_{\text{per}}^i + f_{\text{oc}}^i + f_{\text{sed}}^i$$

and 
$$f_x^i = x_x F_x C_x^{i,\text{melt}}$$

where  $x_x$  is the mass fraction,  $F_x$  the degree of melting,  $C_x^{i,0}$  the trace element composition, and  $\text{IR}_x^i$  the isotopic composition of element  $i$  of each plume component ( $x = \text{per}, \text{oc}, \text{sed}$ ). Hence  $f_x^i = x_x F_x C_x^{i,\text{melt}}$  is the mass fraction of element  $i$  in the melt from each plume component, where  $C_x^{i,\text{melt}}$  is the trace element concentration of the melt.

**Model using new Ce isotope data**

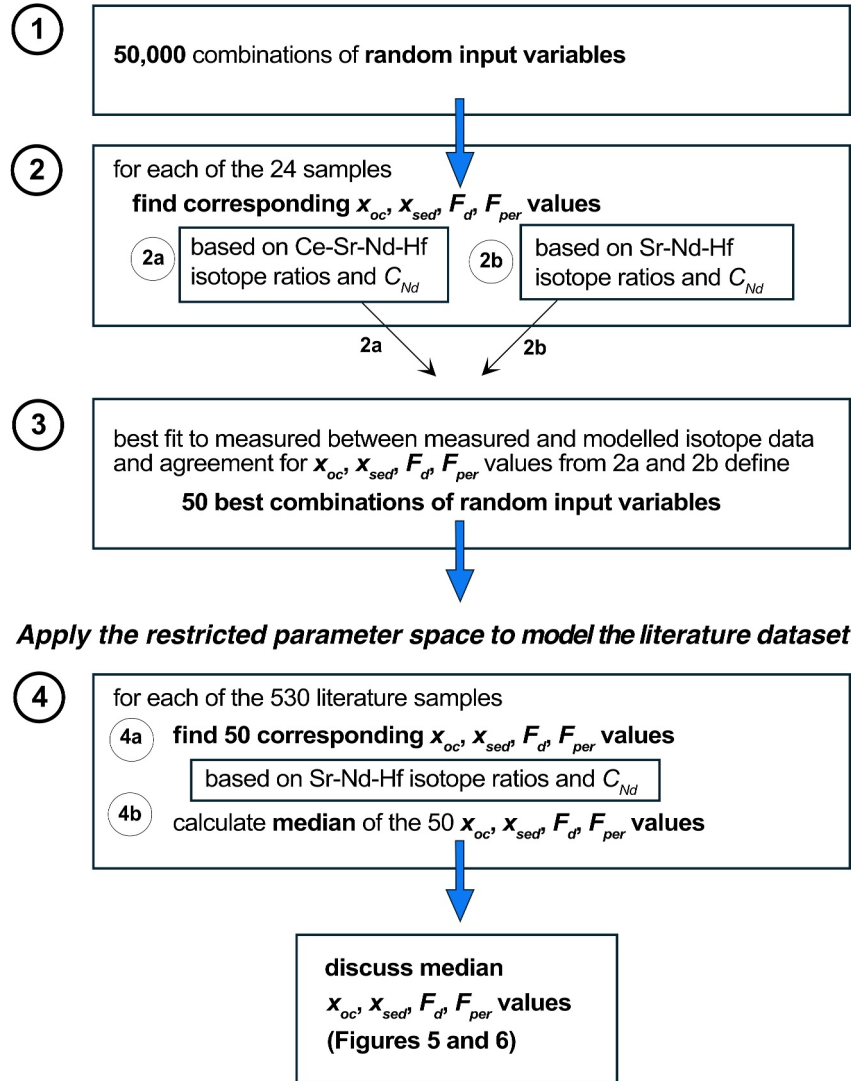


**Figure 4.** Flowchart of the quantitative isotope model. The steps of our general approach as discussed in the text are summarized here.

The compositions of melts from the three plume components,  $C_x^{i\text{ melt}}$ , are calculated using  $C_x^{i,0}$  and the bulk partition coefficients from Pertermann et al. (2004) and Stracke and Bourdon (2009), using accumulated fractional melting (see Table S6 in Supporting Information S2 and Text S1 in Supporting Information S1 for details).

For each *Monte Carlo* simulation, we randomly select the composition of the recycled OC and sediments,  $C_{oc}^i$  and  $C_{sed}^i$ , from a pre-determined compositional range, as well as their degree of melting,  $F_{oc}$  and  $F_{sed}$ , to avoid biasing our model to a specific plume composition (Gale et al., 2013; Plank & Langmuir, 1998; Rudnick & Gao, 2003; Willig et al., 2020; see Text S1 in Supporting Information S1 for details, Tables S3–S5 in Supporting Information S2 for compositions and main Table 1 for the range of randomly selected input compositions and parameters). We assume that the recycled OC and sediments melt to the same extent, that is,  $F_{oc} = F_{sed}$ , which is randomly varied between 0.5 and 0.8. For an initial isotope ratio and randomly selected age of recycling,  $t_{recyc}$  (see Table 1 for input range, and Text S1 in Supporting Information S1 for detailed discussion), and composition,  $C_x^i$ , the present-day isotope ratio of the recycled crust ( $IR_{oc}^i$ ) and sediment ( $IR_{sed}^i$ ) can be calculated with the equation for radioactive decay.

**Table 1**  
*Bounds of Model Parameters*

Name	Equation	Min	Max	Description
Input ranges of randomized, simulation-specific Monte Carlo variables (one value for all samples in a given simulation)				
$t_{recyc}$		1 Ga	2 Ga	Recycling age of the plume components
$t_{cc}$		$t_{recyc}$	3 Ga	Age of the continental crust used in the model
$f_{Gabbro}$	$= x_{Gabbro}/(x_{Gabbro} + x_{Basalt})$	10%	90%	Proportion of gabbro in the recycled mafic crust
$F_{rc}$		50%	80%	Melting degree of the recycled crust in the model (mafic crust and sediments)
Allowed bounds of sample-specific variables calculated by minimizing Equation S7 in Text S1 in Supporting Information S1				
$x_{oc}$		0%	50%	Amount of recycled oceanic crust in the solid plume source of a given sample
$Sed_R$	$= x_{sed}/(x_{oc} + x_{sed})$	0%	50%	Amount of sediments in the total recycled crust (oceanic crust + sediment)
$x_{sed}$	$= Sed_R * x_{oc}/(1 - Sed_R)$			Amount of recycled sediment in the solid plume source of a given sample
$F_d$		0%	15%	Time-integrated degree of peridotite depletion in the solid plume source of a given sample
$F_{per}$		0%	$17\% - F_d$	Degree of melting of plume peridotite during magmatism leading to a given basalt sample

The trace element composition of the peridotite is the depleted mantle of Salters and Stracke (2004), but varies because it melted to different extents before being incorporated into the plume. This prior degree of melting ( $F_d$ ) determines the variable trace element composition of the peridotite ( $C_{per}^i$ ), as well as its isotope ratios after aging during mantle residence, and prior to recent melting in the plume ( $IR_{per}^i$ ). For simplicity, and because compositional variations by far outweigh small variations in initial isotope ratios, we assume that the age of peridotite depletion equals the time of OC and sediment recycling,  $t_{recyc}$ .

Randomly selected variables (e.g., recycling age  $t_{recyc}$ , see Table 1) and plume component compositions take a unique value for each model simulation. There are then four remaining variables that must be determined for constraining plume source composition for each individual sample: (a) the prior degree of peridotite melting before being incorporated into the plume,  $F_d$ , (b) the degree of peridotite melting during recent plume melting ( $F_{per}$ ), and (c) and (d) the abundances of the recycled OC and (d) sediment in the plume source ( $x_{oc}$ ,  $x_{sed}$ , note that the source abundance of the peridotite,  $x_{per} = 1 - x_{oc} - x_{sed}$ ).

These four variables ( $x_{oc}$ ,  $x_{sed}$ ,  $F_d$ ,  $F_{per}$ ) are not selected randomly but can be calculated because Equation 1 can be formulated for four isotope ratios (Sr, Ce, Nd, Hf), which establishes a system of four equations with four independent unknowns that is solved with the minimize function of the *SciPy* package in python (Virtanen et al., 2020). As an additional constraint, we assume that  $C_{basalt}^{Nd}$  is within 10–22  $\mu\text{g/g}$ , similar to primitive Hawaiian lavas (see detailed model description in Text S1 in Supporting Information S1), hence there are 5 equations for 4 unknowns for the samples that have combined Sr-Ce-Nd-Hf isotope ratios. With the additional constraint for  $C_{basalt}^{Nd}$ , the variables  $x_{oc}$ ,  $x_{sed}$ ,  $F_d$ ,  $F_{per}$  can also be calculated if only Sr-Nd-Hf isotope ratios, and  $C_{basalt}^{Nd}$  are used, which is the case for the 530 Hawaiian shield lavas from the literature for which Ce isotope ratios are not available. Further details of the model calculations are given in the Text S1 in Supporting Information S1.

#### 4.1.2. Calculating Hawaiian Plume Composition Through Time

We test 50,000 random plumes, that is, 50,000 combinations of the randomly selected input variables (*Monte Carlo* approach, Table 1, Figure 4), which then constrain the four output variables  $x_{oc}$ ,  $x_{sed}$ ,  $F_d$ ,  $F_{per}$  by minimizing the difference between the predicted and observed Sr-Ce-Nd-Hf isotope ratios for each of the 24 Hawaiian shield lavas with Ce isotope data. For the same 50,000 combinations of input variables, this procedure is repeated without the Ce isotope ratios.

We rate the two sets of  $50,000 \times 24$  solutions against each other using two metrics: *Metric 1* is a “goodness of fit” metric using the sum of root-mean-square deviations between the measured and modeled isotope ratios for the set of 24 Hawaiian shield lavas that have combined Sr-Ce-Nd-Hf isotope ratios (after normalizing isotope values to the measured variance). *Metric 2* measures how close the calculated  $x_{oc}$ ,  $x_{sed}$ ,  $F_d$ ,  $F_{per}$  values determined from

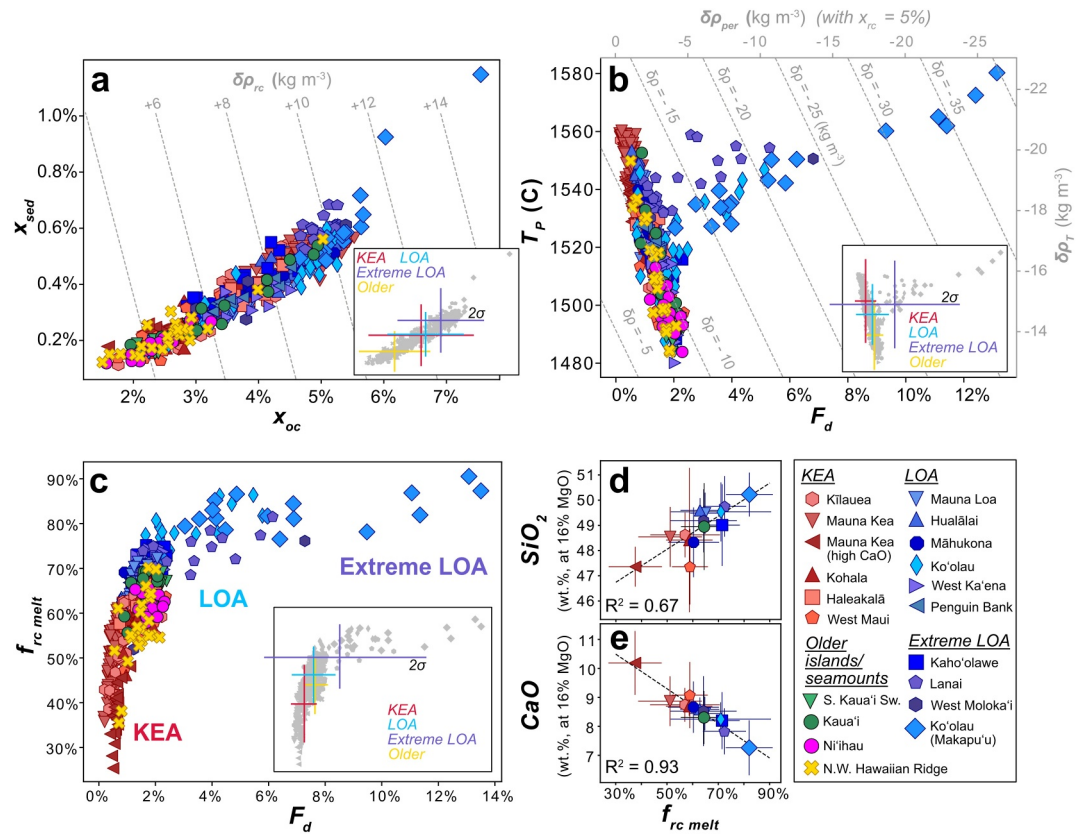


**Figure 5.** Results for plume composition, potential temperature, and melt-mixing proportions. Panel a shows the calculated abundance of recycled oceanic crust (OC) ( $x_{oc}$ ) versus that of recycled sediments ( $x_{sed}$ ) in the plume source (the abundance of peridotite is therefore  $x_{per} = 1 - x_{oc} - x_{sed}$ ). The corresponding excess density due to total recycled crust (rc, OC + sediments) in the plume  $\delta\rho_{rc}$  is shown by the dashed gray lines. Panel b shows the pre-existing degree of peridotite depletion  $F_d$  versus the inferred potential temperature  $T_p$ . The corresponding thermal density deficit,  $\delta\rho_T$ , and compositional density deficit from peridotite depletion  $\delta\rho_{per}$  (assuming  $x_{rc} = 5\%$ , only in this figure) are shown on the right and top axis. The dashed gray lines denote the total density anomaly  $\delta\rho_c = \delta\rho_{rc} + \delta\rho_{per}$ . Panel c shows  $F_d$  versus the proportion of melt from recycled crust in the mixture  $f_{rc\ melt} = ((1 - x_{per}) \cdot F_{rc}) / ((1 - x_{per}) \cdot F_{rc} + x_{per} \cdot F_{per})$ . Panels d and e show correlations between the mean  $f_{rc\ melt}$  for each volcanic center ( $\pm 2\sigma$ ) and the corresponding  $\text{SiO}_2$  and CaO data corrected to 16% MgO (DeFelice et al., 2019; Jackson et al., 2012). The plotted median model results are calculated from the 50 combinations of parameters that best reproduce the isotopic variability of the Hawaiian data as shown in Figure 2. Inserts show the means and two standard deviations ( $2\sigma$ ) of each group of shield lavas (Older islands and seamounts, KEA, LOA, Extreme LOA).

fitting the isotope ratios of the 24 Hawaiian samples with Sr-Ce-Nd-Hf isotope data correspond to the  $x_{oc}$ ,  $x_{sed}$ ,  $F_d$ ,  $F_{per}$  values determined when only the Sr-Nd-Hf isotope ratios are used in the minimization. Applying these two metrics, we determine the best-rated 50 out of all 50,000 simulations (Figure 4).

The resulting 50 different combinations of random input variables (Table S7 in Supporting Information S2) are used for the minimization of the difference between calculated and observed isotope ratios for each of the 530 Hawaiian shield lavas, for which only combined Sr-Nd-Hf isotope data are available. This procedure results in 50 combinations of values for  $x_{oc}$ ,  $x_{sed}$ ,  $F_d$ ,  $F_{per}$  for each of the 530 shield lavas ( $50 \times 530$ ), documenting 47 Myr of Hawaiian plume activity.

Based on the output variables  $x_{oc}$ ,  $x_{sed}$ ,  $F_d$ ,  $F_{per}$  from our geochemical inversion, we compute which plume potential temperature,  $T_p$ , leads to the calculated degree of melting,  $F_{per}$  (for details see model description in Text S1 in Supporting Information S1). We also calculate the thermochemical plume density based on  $T_p$  and the abundance ( $x_x$ ) and density ( $\delta\rho_x$ ) of each plume component (subscript  $x = per, oc, sed$ , see Section 4.2). The median of the 50 values for each variable and each of the 530 shield lavas is plotted in Figures 5 and 6 (i.e.,  $x_{oc}$ ,

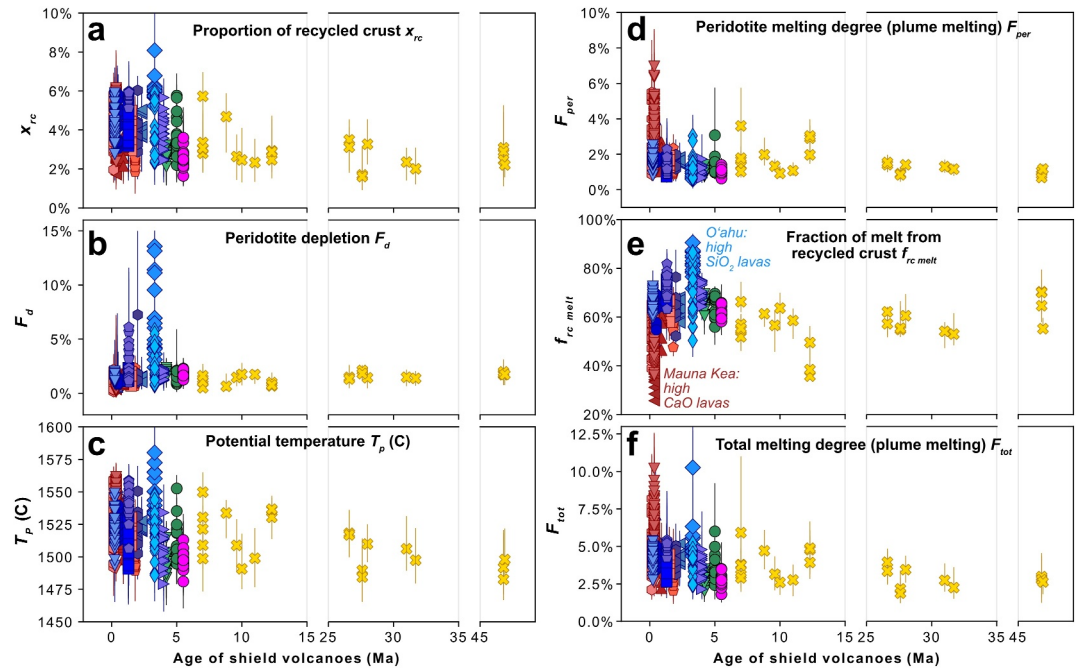


**Figure 6.** Time series plots of model results. Panels show time series plots of (a)  $x_{rc}$ , (b)  $F_d$ , (c)  $T_p$ , (d)  $F_{per}$  (peridotite melting degree during plume magmatism), (e)  $f_{rc\ melt}$  (fraction of melt from recycled crust in the erupted melt mixture), and (f)  $F_{tot}$  (total degree of melting during plume magmatism). Data points are the median model results for each individual sample (symbols as in Figures 1, 2, and 5). Vertical bars show the interquartile range (IQR) around the median. The horizontal axis (age) is truncated between 15–25 Ma and 35–45 Ma as no datapoints are available.

$x_{sed}$ ,  $F_d$ ,  $F_{per}$  and the relative temperature and density variations, see Section 4.2). The bars for each sample in Figure 6 depict the interquartile range (IQR) around the median value of the results.

It should be stressed that our model results are entirely stochastic and not dependent on assumptions beyond the input ranges listed in Table 1 and assuming a three-component plume as described in Section 4.1.1.

#### 4.1.3. Model Results

The results of our inversion constrain the lithological make-up and temperature of the Hawaiian Plume over time. Our results for the 530 lavas of Hawaiian shield volcanism over the last 47 Myr show that the mass fraction of recycled OC in the plume,  $x_{oc}$ , is between ~2% and 6%, and the mass fraction of recycled sediments,  $x_{sed}$ , between ~0.1% and 0.7% (Figure 5a). Therefore, the majority of the plume is made of peridotite ( $x_{per} > 94\%$ ).

The parameters  $x_{oc}$  and  $x_{sed}$  are correlated (Figure 5a), suggesting the proportion of sediment in the recycled crust (rc = oc + sed) is relatively constant. The total mass fraction of recycled crust  $x_{rc}$  ( $= x_{oc} + x_{sed}$ ) varies between ~2% and 6.5%. *Older islands and seamounts* lavas have mean  $x_{rc}$  values of  $3.0\% \pm 1.8\%$  ( $\pm 2\sigma$ ), *KEA* and *LOA* have mean  $x_{rc}$  of  $4.3\% \pm 2.6\%$  and  $4.5\% \pm 1.9\%$ , and *Extreme LOA* lavas have mean  $x_{rc}$  values of  $5.3\% \pm 2.0\%$ .

Importantly, the peridotite component in the plume is characterized by variable extents of prior melt depletion ( $F_d$ ), ranging from 0% to 13% (Figure 5b). Similarly to  $x_{oc}$ ,  $x_{sed}$ , and  $F_{per}$ ,  $F_d$  is a free parameter of the model, meaning the calculated range of  $F_d$  is the sole consequence of a best fit of the calculated and measured isotope ratios. Lower and/or less variable values for  $F_d$  are allowed in our inversion (Table 1), but do not provide the best fit. Values of  $F_d$  of ~13% correspond to peridotites with  $\epsilon_{Hf}$  from 23 to 105, consistent with the  $\epsilon_{Hf}$  values up to 114.5 in peridotite xenoliths from O'ahu, which may represent plume fragments (Bizimis et al., 2007). The Cr number (Cr/(Cr + Al)) of these xenoliths suggests degrees of melt-extraction up to 12% (Bizimis et al., 2007), which agrees well with our results for  $F_d$ . Furthermore, the highest  $\epsilon_{Hf}$  values for the modeled peridotites are found in the source of Makapu'u-stage Ko'olau lavas at O'ahu, concurring with the findings of Salters et al. (2006), who suggest that depleted peridotite is present in the source of Ko'olau. Mean  $F_d$  values are higher in the *Extreme LOA* group ( $F_d = 3.5\% \pm 5.9\%$ ) compared to the other shield lavas (*Older*:  $1.6\% \pm 0.8\%$ , *LOA*:  $1.5\% \pm 1.5\%$ , *KEA*:

0.8% ± 1.0%). Importantly, the range of these latter three groups does not reach the *Extreme LOA* mean, as shown in the inset of Figure 5b, revealing that peridotite depletion is the most distinctive feature of the *Extreme LOA* group.

Because the highly depleted peridotite derived for the source of *Extreme LOA* lavas has a lower melt productivity (see melting parameterization in Text S1 in Supporting Information S1), erupted lavas contain a greater proportion of melt from the recycled crust ( $f_{rc\ melt}$ ) without large changes in the amount of recycled crust in the solid source ( $x_{rc}$ ), or in the melting degree of the latter ( $F_{rc}$ ). This effect is shown in Figure 5c, and is the strongest discriminant between LOA and KEA lavas in our results ( $f_{rc\ melt}$  in KEA: 53% ± 17%, Older: 61% ± 13%, LOA: 65% ± 13%, *Extreme LOA*: 74% ± 15%).

The resulting  $f_{rc\ melt}$  values for individual volcanic centers correlate with their mean SiO<sub>2</sub> and anti-correlate with their mean CaO, corrected to 16% MgO (Figures 5d and 5e) (data from DeFelice et al., 2019; Jackson et al., 2012). The major element variations of Hawaiian shield lavas have been explained as mixing between peridotite melt and melts of pyroxenite/eclogite, which formed from recycled crust with sediment (e.g., Hauri, 1996; Huang & Frey, 2005; Lassiter & Hauri, 1998; Sobolev et al., 2005). Our  $f_{rc\ melt}$  values were estimated based only on isotope compositions. Hence, these correlations (Figures 5d and 5e) provide an additional validation of our model, and explain the distinct major element compositions of Hawaiian lavas. That is, the amount of melt from recycled crust in the erupted lavas is controlled by peridotite depletion (and thus melt productivity) rather than by the amount of recycled crust in the solid source. High CaO lavas from Mauna Kea (DeFelice et al., 2019), for example, sample a peridotite source (Herzberg, 2006) with a low degree of melt-depletion ( $F_d < 1\%$ ). Melts from this high melt productivity peridotite constitute ~70% of the erupted mixture. High SiO<sub>2</sub> lavas from the Makapu'u-stage of Ko'olau sample a peridotite source with a high degree of melt-depletion ( $F_d = 2\%–14\%$ ). Melts from this low melt productivity peridotite constitute ~20% of the erupted mixture, leading to ~80% of the mixture being melts from the recycled crust (Figures 5d and 5e).

#### 4.2. Calculating Plume Potential Temperature and Density

For a fixed final depth or pressure of melting,  $P_f$ , which is constrained by the thickness of the Hawaiian lithosphere (ca. 80 km or  $P_f = 2.6$  GPa), the pressure where melting starts,  $P_o$ , is constrained by the calculated degree of peridotite melting,  $F_{per}$ . Specifically, we calculate the pressure interval  $\Delta P = P_o - P_f$ , that is necessary to get a calculated degree of melting of the peridotitic plume component,  $F_{per}$ . A given value of  $P_o = P_f + \Delta P$  then allows calculating the peridotite solidus temperature  $T_{s,pot}$  for each sample. The peridotite solidus temperature  $T_{s,pot}$  is a function of the starting pressure of melting  $P_o$  and the composition of the peridotite, which is controlled by the variable  $F_d$ . Combining the parameterizations of how potential temperature relates to initial pressure of peridotite melting (Hirschmann, 2000) and peridotite composition (Robinson & Wood, 1998; their Figure 2), we obtain:

$$T_{s,pot}[\text{°C}] = -5.1 \times P_o^2 + 113.9 \times P_o + 1120.7 + 700 \times F_d \quad (2)$$

The plume potential temperature,  $T_p$ , is the sum of (a) the peridotite solidus temperature  $T_{s,pot}$  at the start of melting ( $P_o$ ) and (b) the latent heat of melting of the total recycled crust,  $\delta T_{rc}$  (rc = total recycled crust, i.e., recycled OC plus sediments). Hence,  $T_p$  corresponds to the mantle potential temperature of the plume after correction for the effect of melting recycled crust, whose heat of fusion cools the peridotite.

$$T_p = T_{s,pot} + \delta T_{rc} \quad (3)$$

The latent heat of recycled crust (rc) melting,  $\delta T_{rc}$ , is calculated as follows:

$$\delta T_{rc}[\text{K}] = x_{rc} F_{rc} L / c_p \quad (4)$$

where  $L = 5.6 \times 10^5$  J kg<sup>-1</sup> is the latent heat of the melt for the recycled crust and  $c_p = 1250$  J kg<sup>-1</sup> K<sup>-1</sup> is the specific heat capacity of peridotite.

The plume potential temperature of each sample,  $T_p$ , can be used to calculate the thermal density anomaly,  $\delta\rho_T$ , of the ambient mantle relative to a reference temperature and density:

$$\delta\rho_T[\text{kg m}^{-3}] = -\rho_0 \times \alpha \times (T_p - T_{p\ ref}) \quad (5)$$

where  $\rho_0 = 3,300 \text{ kg m}^{-3}$  is the reference mantle density,  $\alpha = 3 \times 10^{-5} \text{ K}^{-1}$  is the coefficient of thermal expansion, and  $T_{P \text{ ref}} = 1,350^\circ\text{C}$  is the reference mantle potential temperature (Herzberg et al., 2007).

The overall density anomaly of the plume,  $\delta\rho$ , is the sum of the thermal and compositional density anomalies,  $\delta\rho_T$  and  $\delta\rho_c$ , relative to a reference potential temperature and density of the ambient mantle ( $T_{P \text{ ref}} = 1,350^\circ\text{C}$ ,  $\rho = 3,300 \text{ kg m}^{-3}$ ).

The compositional density anomaly,  $\delta\rho_c$ , is calculated from the relative abundances of plume components ( $x_{\text{per}}$ ,  $x_{\text{oc}}$ ,  $x_{\text{sed}}$ ), the density of peridotite,  $\delta\rho_{\text{per}}$ , and the density excess for recycled crust,  $\delta\rho_{\text{rc}}$  (Ishii et al., 2019; Ricolleau et al., 2010). The density of peridotite,  $\delta\rho_{\text{per}}$ , is a function of its extent of melting prior to recent melt extraction during plume melting,  $F_d$ , that is:  $\delta\rho_{\text{per}} = -214.5 \times F_d [\text{kg m}^{-3}]$  (see Afonso & Schutt, 2012).

Estimates of the excess density of recycled OC vary from  $66 \text{ kg m}^{-3}$  (Ricolleau et al., 2010) to  $180 \text{ kg m}^{-3}$  (Ishii et al., 2019). In order to avoid underestimating the influence of dense recycled crust on plume buoyancy in our model, we consider the maximum value of  $180 \text{ kg m}^{-3}$  for the excess density of the recycled crust,  $\delta\rho_{\text{rc}}$ , and for calculating the total compositional density anomaly of the plume,  $\delta\rho_c$ .

Hence:

$$\delta\rho_c = \delta\rho_{\text{rc}} + \delta\rho_{\text{per}} = 180[\text{kg/m}^3] \times x_{\text{rc}} - 214.5[\text{kg/m}^3] \times F_d(1 - x_{\text{rc}}), \quad (6)$$

with  $x_{\text{rc}} = x_{\text{oc}} + x_{\text{sed}}$  being the relative abundance of recycled crust (OC + sediments), and  $1 - x_{\text{rc}} = x_{\text{per}}$ , the abundance of peridotite in the plume.

The total density anomaly of the plume therefore is:

$$\delta\rho = \delta\rho_T + \delta\rho_c = \delta\rho_T + (\delta\rho_{\text{rc}} + \delta\rho_{\text{per}}). \quad (7)$$

Note that the effect of peridotite melting on its density during active plume melting is not considered, as we are interested in the buoyancy of the plume that pushes material into the melting zone and sustains magma flux.

### 4.3. Hawaiian Plume Density

The calculated excess potential temperatures of the Hawaiian Plume,  $\Delta T_p$ , is between  $+130$  and  $+230^\circ\text{C}$  relative to ambient mantle ( $T_{P \text{ ref}} = 1,350^\circ\text{C}$ ; Figure 5b). The mean  $\Delta T_p$  values for the different groups of samples are: *Older*:  $+154 \pm 32^\circ\text{C}$ , *LOA*:  $+173 \pm 28^\circ\text{C}$ , *Extreme LOA*:  $+182 \pm 40^\circ\text{C}$ , *KEA*:  $+186 \pm 39^\circ\text{C}$ . Thus, there is no robust difference in source temperature between the *LOA* and *KEA* side of the hotspot.

The calculated excess potential temperature of the Hawaiian Plume,  $\Delta T_p$ , causes a thermal density deficit  $\delta\rho_T$  between  $-13$  and  $-22 \text{ kg m}^{-3}$  over time (Figure 5b). The compositional density anomaly calculated from the variability of prior melt depletion ( $\delta\rho_{\text{per}}$ ) in the peridotite part of the plume ranges from 0 to  $-26 \text{ kg m}^{-3}$  (Figure 5b), which is an almost three times greater range than for  $\delta\rho_T$ . The compositional density anomaly associated with recycled crust,  $\delta\rho_{\text{rc}}$ , ranges from  $+3.5$  to  $+16 \text{ kg m}^{-3}$  (Figure 5a). This comparatively small  $\delta\rho_{\text{rc}}$  is an upper bound, because a lower density of the recycled OC, such as the  $66 \text{ kg m}^{-3}$  of Ricolleau et al. (2010), would yield a maximum  $\delta\rho_{\text{rc}}$  of only  $+5.7$  instead of  $+16 \text{ kg m}^{-3}$ .

Hence, in good agreement with previous studies, the Hawaiian plume is significantly hotter than ambient mantle. The excess temperature of the Hawaiian plume compensates the excess density ( $\delta\rho_{\text{rc}}$ ) of small amounts ( $\lesssim 6\%$ ) of recycled crust in the plume (Figure 5a). But depleted peridotite adds a significant density deficit to the plume (Figure 5b; Equation 7). The density deficit caused by peridotite depletion can outweigh the excess density of the recycled crust, even though we assume the maximum excess density for the recycled crust. Hence, peridotite melt depletion prior to incorporation into the plume can increase plume buoyancy and provide an additional or alternative source to excess temperature for driving plume upwelling. In detail, our calculation shows that the additional buoyancy provided by depleted peridotite can be as large as that provided by thermal buoyancy.

For most of the Hawaiian plume volcanism, the small variations in the abundance of recycled OC (ca. 2%–6%) and sediment (ca. 0.1%–0.7%, Figure 5a) in combination with the relatively constant extent of pre-existing degree of peridotite depletion  $F_d$  (ca. 1%–3%, Figure 5b) and plume potential temperatures result in relatively constant

thermochemical plume density and thus plume buoyancy. However, exceptionally high values of peridotite melt depletion prior to incorporation into the plume ( $F_d$  ca. >4% and up to ca. 13%) can significantly decrease plume density, and thus increase plume buoyancy (Figure 5b).

Group-specific plume density anomalies are  $\delta\rho = -12.5 \pm 2.9 \text{ kg m}^{-3}$  for *KEA* lavas and  $\delta\rho = -12.3 \pm 3.0 \text{ kg m}^{-3}$  for *LOA* lavas. *Extreme LOA* lavas show density anomalies of  $\delta\rho = -15.8 \pm 12.2 \text{ kg m}^{-3}$ , while *Older* lavas have  $\delta\rho = -13.4 \pm 2.3 \text{ kg m}^{-3}$ , however with a value of  $\delta\rho = -18 \text{ kg m}^{-3}$  at 15 Ma. A large decrease in plume density occurs simultaneously to the observed burst in magma production at 1 to 3 Ma (Van Ark & Lin, 2004; Vidal & Bonneville, 2004; Wessel, 2016). In the following, we show that the decreased plume density and therefore increased plume buoyancy due to intermittent upwelling of highly depleted peridotite accelerates plume upwelling rate, which increases plume volume flux and thus magma volume flux sufficiently to explain the observed burst in magma production at <3 Ma.

#### 4.4. Hawaiian Plume Buoyancy, Plume and Magma Volume Flux

Figures 5a and 5b show that the differences in overall calculated plume density,  $\delta\rho$ , are mostly controlled by the different extents of peridotite depletion ( $F_d$ ) rather than by potential temperature ( $T_p$ ). Less dense and thus more buoyant peridotite accelerates plume upwelling, increasing plume volume flux and magma production rate (magma volume flux). The time-series plots in Figures 6a–6c show that  $T_p$  and the proportion of recycled crust ( $x_{rc}$ ) remain relatively constant through time, while  $F_d$  peaks between 1 and 3 Ma.

To test whether buoyancy variations due to depleted and lighter peridotite in the plume suffice to explain bursts in Hawaiian magma production, we calculate the plume upwelling velocity,  $v_p$ , the plume volume flux per time,  $Q_p$ , and the magma volume flux per time,  $Q_v$ , from the calculated  $\delta\rho$  of each sample as follows:

According to Stokes' Law, the upwelling velocity  $v_p$  relates to  $\delta\rho$  by:

$$v_p = -\frac{2}{9}\delta\rho g r^2 \eta^{-1} \quad (8)$$

where  $v_p$  is in  $\text{m s}^{-1}$ ,  $\delta\rho$  is the total density difference between the plume and ambient mantle in  $\text{kg m}^{-3}$  (see above),  $\eta$  is the asthenospheric viscosity in Pa s,  $g$  in  $\text{m s}^{-2}$  is Earth's gravitational acceleration, and  $r$  is the radius of the upwelling plume in m.

From  $v_p$ , the plume volume flux per time,  $Q_p$ , can then be scaled as follows:

$$Q_p = v_p r^2 \pi \left[ \text{m}^3 \text{ s}^{-1} \right] \quad (9)$$

where  $Q_p$  is in  $\text{m}^3 \text{ s}^{-1}$  and  $r$  is the radius of the upwelling plume in m.

From  $Q_p$ , the magma volume flux,  $Q_v$ , can be calculated:

$$Q_v = Q_p \frac{\rho_0}{\rho_{\text{melt}}} F_{\text{total}} \left[ \text{m}^3 \text{ s}^{-1} \right] \quad (10)$$

where  $\rho_0 = 3,300 \text{ kg m}^{-3}$  is the reference mantle density, and  $\rho_{\text{melt}} = 2,900 \text{ kg m}^{-3}$  is the density of an erupted basalt, and  $F_{\text{total}}$  is the total degree of plume melting (see details in Text S1 in Supporting Information S1).

Magma volume flux is thus a function of both the plume volume flux  $Q_p$  and the melting degree  $F_{\text{tot}}$ . Our model results show that the extent of peridotite melting,  $F_{\text{per}}$  (plume melting), is relatively constant, with a sharp increase in the most recent (<1 Ma) *KEA* lavas of Mauna Kea and Kilauea (Figure 6d). This increase in  $F_{\text{per}}$  causes  $f_{\text{rc melt}}$  to decrease if  $x_{rc} \ll x_{\text{per}}$  and  $F_{\text{tot}}$  to increase sharply (Figures 6e and 6f). This effect is explained quantitatively with a simple example in Text S1 in Supporting Information S1 (Section 1.5 therein).

Figure 7a shows a time-series plot for our resulting values for  $Q_p$ . Variations in  $F_d$  cause  $Q_p$  to increase 3-fold from  $100 \text{ m}^3 \text{ s}^{-1}$  to  $334 \text{ m}^3 \text{ s}^{-1}$  at 1 to 3 Ma in the *Extreme LOA*. This increase is almost entirely driven by increasing  $F_d$ , as shown in Figure 7b. We find that  $F_d$  controls  $Q_v$  through two distinct processes (Figure 7c; Equation 10): (a) high values of  $F_d$  in *Extreme LOA* lavas cause  $Q_p$  to increase, resulting in a higher flux of

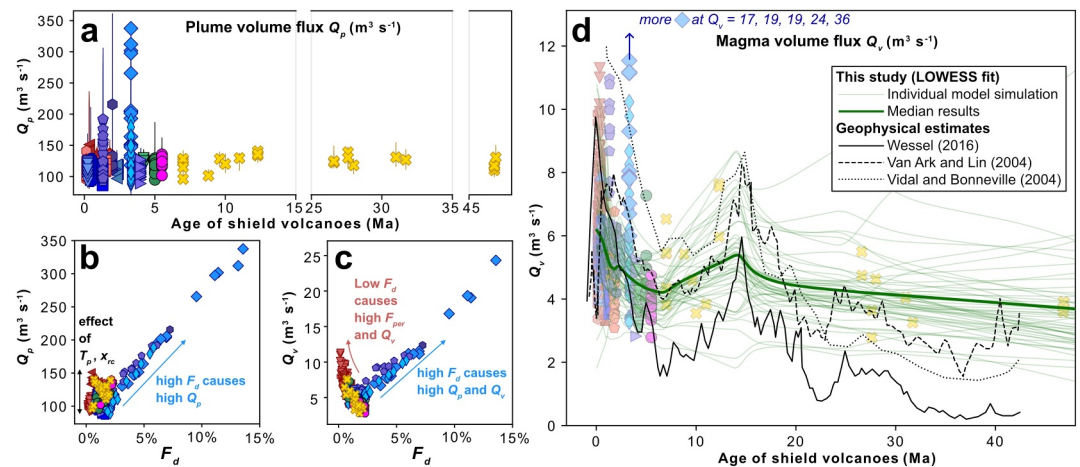


**Figure 7.** Time series plots of plume and magma flux and correlations with  $F_d$ . Panel (a) shows a time series of  $Q_p$  (plume volume flux). Datapoints and vertical bars as in Figure 6. Panels (b) and (c) display the correlation between peridotite depletion  $F_d$  and plume volume flux  $Q_p$  and magma volume flux  $Q_v$ . Panel (d) shows a time series of  $Q_v$  (magma volume flux). Symbols show median results, while thin green curves show LOcally WEighted Scatterplot Smoothing (LOWESS) fits through each of the 50 best solutions. The thick green curve shows a LOWESS fit through all median results. LOWESS fits have a smoothing parameter of 0.667. Black curves represent literature geophysical estimates of  $Q_v$ , calculated by estimating the volume of magma required to generate the seamounts of the Hawaiian Emperor seamount chain (Van Ark & Lin, 2004; Vidal & Bonneville, 2004; Wessel, 2016). The three literature profiles are correlated in time as done by Wessel (2016). Linear regression parameters between our LOWESS fit and the geophysical curves are shown in Table S8 in Supporting Information S2.

material into the melting zone (Equation 10), and (b) the lowest values of  $F_d$  in Mauna Kea and Kilauea lavas cause an increase in  $F_{tot}$  due to higher peridotite melt productivity (Equation 10). Hence the magma volume flux,  $Q_v$ , can increase either because the plume volume flux per time,  $Q_p$ , increases due to increased buoyancy of the plume (scenario 1), or,  $Q_v$  can increase because higher melt productivity of the major plume component (peridotite) increases  $F_{per}$  and thus  $F_{tot}$  at a given plume volume flux per time,  $Q_p$  (Equation 10).

Our calculated  $Q_v$  match geophysical  $Q_v$  estimates (Van Ark & Lin, 2004; Vidal & Bonneville, 2004; Wessel, 2016) (Figure 7d) for a plume radius  $r = 70$  km and a viscosity  $\eta = 1.8 \times 10^{19}$  Pa·s (Ballmer et al., 2011) (solid green curve in Figure 7d), yielding a maximum upwelling velocity  $v_p = 68$  cm yr<sup>-1</sup> ( $v_p$  in Table S2 in Supporting Information S2). For these  $r$  and  $\eta$ , fully coupled numerical models of plume-lithosphere interaction predict Hawaiian swell shapes and geographical melt distributions consistent with observations (see Ballmer et al., 2011). We note that other combinations of  $r$  and  $\eta$  give different absolute values of  $Q_v$ , but the same relative  $Q_v$  versus time patterns, which are entirely constrained by our geochemical inversion.

In order to quantify the fit between our  $Q_v$  results and geophysical estimates we regress our inferred  $Q_v$  values as a function of time using LOcally WEighted Scatterplot Smoothing (Figure 7d) and compare the resulting curve with those for published geophysical estimates of  $Q_v$  (Van Ark & Lin, 2004; Vidal & Bonneville, 2004; Wessel, 2016). Regressions between our results and these estimates yield  $R^2$  coefficients between 0.7 and 0.83, similar to the fit between any two sets of these geophysical estimates (0.75–0.91) (see Table S8 in Supporting Information S2).

Our isotope-derived model results therefore readily explain the full range of  $Q_v$  variations observed for the past 47 Myr of plume activity and, in particular, the recent burst in magma volume flux at <3 Ma (Figure 7d). The increase in plume volume flux  $Q_p$  caused by the upwelling of buoyant, melt-depleted (high  $F_d$ ) peridotite at 1 to 3 Ma initially caused this burst in  $Q_v$ . This burst is sustained in the most recent lavas (<1 Ma) by oscillation back to melting less melt-depleted peridotite, that is, very low  $F_d$  values, causing a sharp increase in  $F_{tot}$  at that time. Our model results for the few samples modeled at 10 to 15 Ma are also consistent with the increase of  $Q_v$  observed by geophysical estimates for that period.

While we do not rule out that variations in plume temperature and/or radius may contribute to  $Q_v$  variability, as has been previously proposed for the Pūhāhonu volcano (Garcia et al., 2020), our results suggest that variably

depleted peridotite in the plume largely controls magma volume flux, causing bursts of activity that are geochemically and geophysically detectable.

Indeed, the availability of compositionally light materials such as depleted peridotite affects plume development and entrainment, and thereby the geometry of upwelling plumes (Tackley, 2011). In this context, complex plume geometries such as “fat” plumes and plume branching may be related to different contents of variably depleted-peridotite in the plume and lower-mantle rheology instead of recycled crust entrainment as previously thought (Davaille et al., 2018; Kumagai et al., 2008). In particular, our results suggest that incorporation of strongly depleted peridotite (i.e., most clearly evident in the 1 to 3 Ma Hawaiian lavas; Figure 6b) can trigger a sustained plume pulse and a surge in volcanic activity that lasts until today.

Overall, the approach developed in this study shows that radiogenic isotope data in oceanic basalts can be related to geophysical and geochemical properties of the underlying mantle in an explicit, quantitative manner. Using the combined Sr-Ce-Nd-Hf isotope ratios has been instrumental for identifying variably depleted peridotite in the Hawaiian plume, and hence for unraveling that the transient upwelling of more incompatible element depleted mantle made the Hawaiian plume intermittently lighter and more buoyant. This effect led to an increase in magma volume flux at ~1–3 Ma, which led to the emergence of the Hawaiian Islands.

#### 4.5. Implications for Developing the Hawaiian Double Chain Volcanism

The large plume volume flux increase at ~1–3 Ma (Figure 7a) coincides with the appearance of a double chain in Hawai‘i, where two loci of volcanism are active simultaneously (Figure 1b). This timing of events implies a new geodynamical hypothesis for the origin of the *LOA-KEA* double chain, although formal testing goes beyond the scope of the present study. Namely, that the increasing plume volume flux at ~1–3 Ma may have resulted in plume material spreading laterally across the plume track to accommodate the excessive upwelled volume. This may in turn have resulted in a lateral widening of the mantle melting zone. Volcanic loading can guide and focus melts from different parts of the wide melting region into two alternating volcanic plumbing systems such as those of Loa and Kea volcanoes (Hieronymus & Bercovici, 1999). This effect may have occurred in combination with other previously proposed mechanisms for double chain formation such as small-scale convection and tilting of the plume (Ballmer et al., 2011; Bianco et al., 2008; Jones et al., 2017).

#### 4.6. Further Implications for Global OIB (Ocean Island Basalts) Volcanism

Plume buoyancy variations due to variably depleted peridotite may not only control the temporal patterns of volcanic activity of the Hawaiian plume, but also those of other plumes world-wide. Indeed, plate subduction and slab sinking conveys up to ~400 km<sup>3</sup> Myr<sup>-1</sup> of variably depleted peridotites into the mantle (Hounslow et al., 2018), and a significant fraction ends up in the lowermost mantle (Tauzin et al., 2022). Their excess compositional buoyancy will readily trigger upwelling (Tackley, 2011), and thus sustain active upwelling of comparatively cool mantle, so-called “cold plumes” (Sanfilippo et al., 2024; Shorttle et al., 2014; Stracke & Béguelin, 2024; Stracke et al., 2019, 2022). Indeed, buoyancy fluxes of plume-fed hotspots do not correlate well with seismically inferred plume temperatures (Bao et al., 2022) (Figure S4 in Supporting Information S1), consistent with our findings that an additional buoyancy source is required. Buoyancy differences caused by variable depletion of peridotite are therefore a critical, but so far underappreciated parameter for convective mantle flow (Sanfilippo et al., 2024; Stracke & Béguelin, 2024; Stracke et al., 2019, 2022), in good agreement with recent global-scale geodynamic models (Tucker et al., 2022).

Our results also imply that contrary to common notion (e.g., White, 2010 and references therein), the actively upwelling mantle under most OIB locations possibly contains a greater proportion and/or more incompatible element depleted peridotite than the sub-ridge mantle (Sanfilippo et al., 2024; Stracke & Béguelin, 2024; Stracke et al., 2019, 2022). In this case, the relative contribution from the incompatible element depleted peridotite to the weighted average of the aggregated melts is comparatively low (Figure 5c), so that melts from volumetrically minor, but incompatible element enriched source components, such as recycled oceanic and continental crust, dominate the Sr-Ce-Nd-Hf-Pb isotope ratios of the erupted melts (e.g., Stracke & Béguelin, 2024; Willig et al., 2020) (Figures 2 and 3, Equation 1). This may explain why Hawaiian basalts, and plume-derived OIB in general, have on average lower Nd, Hf and higher Sr, Ce isotope ratios than MORB (Stracke & Béguelin, 2024; Stracke et al., 2019, 2022). In Hawaii, this effect causes the *Extreme LOA* lavas to have markedly more enriched isotope values compared to the rest of the *LOA* group (Figures 2 and 3).

If the source of OIB indeed contains, on average, more incompatible element depleted peridotite than the sub-ridge mantle, the major peridotite component of OIB mantle sources may also contain less U-Th, and thus accumulate less  $^4\text{He}$  over time by  $\alpha$ -decay than the mantle sources of MORB. Recycled oceanic and continental crust is nearly devoid of He (Hilton & Porcelli, 2014), but rich in U-Th. Variable  $^4\text{He}$  due to  $\alpha$ -decay of U-Th may therefore play a greater role for the  $^3\text{He}/^4\text{He}$  variability in MORB and OIB (Parman, 2007) compared to  $^3\text{He}$  variation due to variable mantle degassing than previously thought (e.g., Hilton & Porcelli, 2014). This decoupling may explain why most OIB suites extend to higher  $^3\text{He}/^4\text{He}$  (e.g., Class & Goldstein, 2005; Hilton & Porcelli, 2014; Parman, 2007), but also lower  $^3\text{He}/^{36}\text{Ar}$  and  $^3\text{He}/^{22}\text{Ne}$  than MORB (Hilton & Porcelli, 2014; Moreira, 2013; Parai, 2025; Stracke, 2025; and references in these studies). Ocean island basalts ranging to the highest observed  $^3\text{He}/^4\text{He}$  such as those from Hawaii and Iceland (Hilton & Porcelli, 2014; Jackson et al., 2021; Parman, 2007), may therefore contain some of the mantle's most incompatible element depleted peridotite (Hawaii: *this study*, Iceland: Sanfilippo et al., 2024). Indeed, previous work has established a correlation between maximum  $^3\text{He}/^4\text{He}$  and plume buoyancy flux at a given hotspot (Jackson et al., 2017, 2021), indicating that upwelling of vigorous plumes with large hotspot swells may be promoted by depleted peridotite in the source, that is characterized by high  $^3\text{He}/^4\text{He}$  (low U, Th, and thus low  $^4\text{He}$ , e.g., Class & Goldstein, 2005; Dygert et al., 2018; Parman, 2007; Stracke, 2025), and low density and is thus compositionally buoyant.

### Conflict of Interest

The authors declare no conflicts of interest relevant to this study.

### Data Availability Statement

All data generated and analyzed in the present study are included in the Supplementary Tables. The data generated in the present study is available on the GEOROC database at (Béguelin, 2025b).

### Code Availability

The *Python* code used in the present study is archived on *Zenodo* at (Béguelin, 2025a).

### Acknowledgments

P.B. acknowledges funding through Early Postdoc.Mobility Grant P2SKP2\_187642 from the Swiss National Science Foundation, Short-Term Research Grant 57552337 from the German Academic Exchange Service, and SPARC Grant 21610-18-46611 from the University of South Carolina. A.S. acknowledges funding through DFG grant STR853/9-1. M. Ballmer acknowledges NERC Grant NE/X000508/1. M. Bizimis acknowledges funding through Grant NSF-OCE 1624315. P.B. thanks H. Baier and M. Böhnke for help with mass spectrometry, and A. Plimmer for scientific discussions. We are grateful for the reviews of Stephen Parman and two anonymous reviewers whose comments greatly improved this article. Open Access funding enabled and organized by Projekt DEAL.

### References

- Abouchami, W., Hofmann, A. W., Galer, S. J. G., Frey, F. A., Eisele, J., & Feigenson, M. (2005). Lead isotopes reveal bilateral asymmetry and vertical continuity in the Hawaiian mantle plume. *Nature*, *434*(7035), 851–856. <https://doi.org/10.1038/nature03402>
- Afonso, J. C., & Schutt, D. L. (2012). The effects of polybaric partial melting on density and seismic velocities of mantle restites. *Lithos*, *134*, 289–303. <https://doi.org/10.1016/j.lithos.2012.01.009>
- Asimow, P. D., Hirschmann, M. M., & Stolper, E. M. (1997). An analysis of variations in isentropic melt productivity. *Philosophical Transactions of the Royal Society of London, Series A: Mathematical, Physical and Engineering Sciences*, *355*(1723), 255–281. <https://doi.org/10.1098/rsta.1997.0009>
- Ballmer, M. D., Ito, G., Van Hunen, J., & Tackley, P. J. (2011). Spatial and temporal variability in Hawaiian hotspot volcanism induced by small-scale convection. *Nature Geoscience*, *4*(7), 457–460. <https://doi.org/10.1038/ngeo1187>
- Bao, X., Lithgow-Bertelloni, C. R., Jackson, M. G., & Romanowicz, B. (2022). On the relative temperatures of Earth's volcanic hotspots and mid-ocean ridges. *Science*, *375*(6576), 57–61. <https://doi.org/10.1126/science.abj8944>
- Béguelin, P. (2025a). Code for the article “Variations in Hawaiian plume flux controlled by ancient mantle depletion” (v.1.0.0). *Zenodo*. <https://doi.org/10.5281/zenodo.14814639>
- Béguelin, P. (2025b). Data from the article Variations in Hawaiian plume flux controlled by ancient mantle depletion [Dataset] GRO.data, V1, UNF:6:p/nthdsDl2Gv6OGLgzbAlg== [fileUNF]. <https://doi.org/10.25625/BZYLZO>
- Béguelin, P., Bizimis, M., Beier, C., & Turner, S. (2017). Rift–plume interaction reveals multiple generations of recycled oceanic crust in Azores lavas. *Geochimica et Cosmochimica Acta*, *218*, 132–152. <https://doi.org/10.1016/j.gca.2017.09.015>
- Béguelin, P., Bizimis, M., McIntosh, E. C., Cousens, B., & Clague, D. A. (2019). Sources vs processes: Unraveling the compositional heterogeneity of rejuvenated-type Hawaiian magmas. *Earth and Planetary Science Letters*, *514*, 119–129. <https://doi.org/10.1016/j.epsl.2019.03.011>
- Bianco, T. A., Ito, G., van Hunen, J., Ballmer, M. D., & Mahoney, J. J. (2008). Geochemical variation at the Hawaiian hot spot caused by upper mantle dynamics and melting of a heterogeneous plume. *Geochemistry, Geophysics, Geosystems*, *9*(11), Q11003. <https://doi.org/10.1029/2008gc002111>
- Bizimis, M., Griselin, M., Lassiter, J. C., Salters, V. J., & Sen, G. (2007). Ancient recycled mantle lithosphere in the Hawaiian plume: Osmium–hafnium isotopic evidence from peridotite mantle xenoliths. *Earth and Planetary Science Letters*, *257*(1–2), 259–273. <https://doi.org/10.1016/j.epsl.2007.02.036>
- Bizimis, M., Sen, G., Salters, V. J., & Keshav, S. (2005). Hf–Nd–Sr isotope systematics of garnet pyroxenites from Salt Lake Crater, Oahu, Hawaii: Evidence for a depleted component in Hawaiian volcanism. *Geochimica et Cosmochimica Acta*, *69*(10), 2629–2646. <https://doi.org/10.1016/j.gca.2005.01.005>
- Blichert-Toft, J., Frey, F. A., & Albarede, F. (1999). Hf isotope evidence for pelagic sediments in the source of Hawaiian basalts. *Science*, *285*(5429), 879–882. <https://doi.org/10.1126/science.285.5429.879>

- Bouvier, A., Vervoort, J. D., & Pachtet, P. J. (2008). The Lu–Hf and Sm–Nd isotopic composition of CHUR: Constraints from unequilibrated chondrites and implications for the bulk composition of terrestrial planets. *Earth and Planetary Science Letters*, 273(1–2), 48–57. <https://doi.org/10.1016/j.epsl.2008.06.010>
- Byerly, B. L., & Lassiter, J. C. (2014). Isotopically ultradepleted domains in the convecting upper mantle: Implications for MORB petrogenesis. *Geology*, 42(3), 203–206. <https://doi.org/10.1130/g34757.1>
- Campbell, I. H. (2007). Testing the plume theory. *Chemical Geology*, 241(3–4), 153–176. <https://doi.org/10.1016/j.chemgeo.2007.01.024>
- Chauvel, C., Lewin, E., Carpentier, M., Arndt, N. T., & Marini, J. C. (2008). Role of recycled oceanic basalt and sediment in generating the HF–Nd mantle array. *Nature Geoscience*, 1(1), 64–67. <https://doi.org/10.1038/ngeo.2007.51>
- Clague, D. A., & Dalrymple, G. B. (1987). *The Hawaiian-Emperor volcanic chain, part 1, geologic evolution* (pp. 5–54). U.S. Geological Survey Professional Paper 1350.
- Clague, D. A., & Frey, F. A. (1982). Petrology and trace element geochemistry of the Honolulu volcanics, Oahu: Implications for the oceanic mantle below Hawaii. *Journal of Petrology*, 23(3), 447–504. <https://doi.org/10.1093/petrology/23.3.447>
- Clague, D. A., & Sherrod, D. R. (2014). Growth and degradation of Hawaiian volcanoes. *Characteristics of Hawaiian volcanoes, 1801*, 97–146. <https://doi.org/10.3133/pp18013>
- Class, C., & Goldstein, S. L. (2005). Evolution of helium isotopes in the Earth's mantle. *Nature*, 436(7054), 1107–1112. <https://doi.org/10.1038/nature03930>
- Cousens, B. L., & Clague, D. A. (2015). Shield to rejuvenated stage volcanism on Kauai and Niihau, Hawaiian Islands. *Journal of Petrology*, 56(8), 1547–1584. <https://doi.org/10.1093/petrology/egv045>
- d'Acremont, E., Leroy, S., & Burov, E. B. (2003). Numerical modelling of a mantle plume: The plume head–lithosphere interaction in the formation of an oceanic large igneous province. *Earth and Planetary Science Letters*, 206(3–4), 379–396. [https://doi.org/10.1016/s0012-821x\(02\)01058-0](https://doi.org/10.1016/s0012-821x(02)01058-0)
- Davaillé, A., Carrez, P., & Cordier, P. (2018). Fat plumes may reflect the complex rheology of the lower mantle. *Geophysical Research Letters*, 45(3), 1349–1354. <https://doi.org/10.1002/2017gl076575>
- David, K., Schiano, P., & Allegre, C. J. (2000). Assessment of the Zr/Hf fractionation in oceanic basalts and continental materials during petrogenetic processes. *Earth and Planetary Science Letters*, 178(3–4), 285–301. [https://doi.org/10.1016/S0012-821X\(00\)00088-1](https://doi.org/10.1016/S0012-821X(00)00088-1)
- Davis, M. G., Garcia, M. O., & Wallace, P. (2003). Volatiles in glasses from Mauna Loa Volcano, Hawai'i: Implications for magma degassing and contamination, and growth of Hawaiian volcanoes. *Contributions to Mineralogy and Petrology*, 144(5), 570–591. <https://doi.org/10.1007/s00410-002-0416-z>
- DeFelice, C., Mallick, S., Saal, A. E., & Huang, S. (2019). An isotopically depleted lower mantle component is intrinsic to the Hawaiian mantle plume. *Nature Geoscience*, 12(6), 487–492. <https://doi.org/10.1038/s41561-019-0348-0>
- Dixon, J., Clague, D. A., Cousens, B., Monsalve, M. L., & Uhl, J. (2008). Carbonatite and silicate melt metasomatism of the mantle surrounding the Hawaiian plume: Evidence from volatiles, trace elements, and radiogenic isotopes in rejuvenated-stage lavas from Niihau, Hawaii. *Geochemistry, Geophysics, Geosystems*, 9(9), Q09005. <https://doi.org/10.1029/2008gc002076>
- Dyger, N., Jackson, C. R., Hesse, M. A., Tremblay, M. M., Shuster, D. L., & Gu, J. T. (2018). Plate tectonic cycling modulates Earth's 3He/22Ne ratio. *Earth and Planetary Science Letters*, 498, 309–321. <https://doi.org/10.1016/j.epsl.2018.06.044>
- Farnetani, C. G., & Samuel, H. (2005). Beyond the thermal plume paradigm. *Geophysical Research Letters*, 32(7), L07311. <https://doi.org/10.1029/2005gl022360>
- Fekiacova, Z., Abouchami, W., Galer, S. J. G., Garcia, M. O., & Hofmann, A. W. (2007). Origin and temporal evolution of Ko'olau Volcano, Hawai'i: Inferences from isotope data on the Ko'olau Scientific Drilling Project (KSDP), the Honolulu Volcanics and ODP Site 843. *Earth and Planetary Science Letters*, 261(1–2), 65–83. <https://doi.org/10.1016/j.epsl.2007.06.005>
- Flanagan, F. J. (1973). *Descriptions and analyses of eight new USGS rock standards*. US Government Printing Office.
- Fodor, R. V., & Moore, R. B. (1994). Petrology of gabbroic xenoliths in 1960 Kilauea basalt: Crystalline remnants of prior (1955) magmatism. *Bulletin of Volcanology*, 56(1), 62–74. <https://doi.org/10.1007/s004450050017>
- French, S. W., & Romanowicz, B. A. (2014). Whole-mantle radially anisotropic shear velocity structure from spectral-element waveform tomography. *Geophysical Journal International*, 199(3), 1303–1327. <https://doi.org/10.1093/gji/ggu334>
- Frey, F. A., Clague, D., Mahoney, J. J., & Sinton, J. M. (2000). Volcanism at the edge of the Hawaiian plume: Petrogenesis of submarine alkalic lavas from the North Arch volcanic field. *Journal of Petrology*, 41(5), 667–691. <https://doi.org/10.1093/petrology/41.5.667>
- Frey, F. A., Huang, S., Blichert-Toft, J., Regelous, M., & Boyet, M. (2005). Origin of depleted components in basalt related to the Hawaiian hotspot: Evidence from isotopic and incompatible element ratios. *Geochemistry, Geophysics, Geosystems*, 6(2), Q02L07. <https://doi.org/10.1029/2004gc000757>
- Frey, F. A., Huang, S., Xu, G., & Jochum, K. P. (2016). The geochemical components that distinguish Loa-and Kea-trend Hawaiian shield lavas. *Geochimica et Cosmochimica Acta*, 185, 160–181. <https://doi.org/10.1016/j.gca.2016.04.010>
- Gaffney, A. M., Nelson, B. K., & Blichert-Toft, J. (2004). Geochemical constraints on the role of oceanic lithosphere in intra-volcano heterogeneity at West Maui, Hawaii. *Journal of Petrology*, 45(8), 1663–1687. <https://doi.org/10.1093/petrology/egh029>
- Gaffney, A. M., Nelson, B. K., & Blichert-Toft, J. (2005). Melting in the Hawaiian plume at 1–2 Ma as recorded at Maui Nui: The role of eclogite, peridotite, and source mixing. *Geochemistry, Geophysics, Geosystems*, 6(10). <https://doi.org/10.1029/2005gc000927>
- Gale, A., Dalton, C. A., Langmuir, C. H., Su, Y., & Schilling, J. G. (2013). The mean composition of ocean ridge basalts. *Geochemistry, Geophysics, Geosystems*, 14(3), 489–518. <https://doi.org/10.1029/2012GC004334>
- Garcia, M. O., Swinnard, L., Weis, D., Greene, A. R., Tagami, T., Sano, H., & Gandy, C. E. (2010). Petrology, geochemistry and geochronology of Kaua'i lavas over 4–5 Myr: Implications for the origin of rejuvenated volcanism and the evolution of the Hawaiian plume. *Journal of Petrology*, 51(7), 1507–1540. <https://doi.org/10.1093/petrology/egq027>
- Garcia, M. O., Tree, J. P., Wessel, P., & Smith, J. R. (2020). Pūhāhonu: Earth's biggest and hottest shield volcano. *Earth and Planetary Science Letters*, 542, 116296. <https://doi.org/10.1016/j.epsl.2020.116296>
- Garcia, M. O., Weis, D., Swinnard, L., Ito, G., & Pietruszka, A. J. (2015). Petrology and geochemistry of volcanic rocks from the South Kauai swell volcano, Hawaii: Implications for the lithology and composition of the Hawaiian mantle plume. *Journal of Petrology*, 56(6), 1173–1197. <https://doi.org/10.1093/petrology/egv033>
- Green, D. H., & Falloon, T. J. (2005). Primary magmas at mid-ocean ridges “hotspots”, and other intraplate settings: Constraints on mantle potential temperature. *Geological Society of America Special Paper*, 388, 217–247.
- Greene, A. R., Garcia, M. O., Weis, D., Ito, G., Kuga, M., Robinson, J., & Yamasaki, S. (2010). Low-productivity Hawaiian volcanism between Kaua'i and O'ahu. *Geochemistry, Geophysics, Geosystems*, 11(11). <https://doi.org/10.1029/2010gc003233>
- Griffiths, R. W., & Campbell, I. H. (1990). Stirring and structure in mantle starting plumes. *Earth and Planetary Science Letters*, 99(1–2), 66–78. [https://doi.org/10.1016/0012-821x\(90\)90071-5](https://doi.org/10.1016/0012-821x(90)90071-5)

- Hanyu, T., Kimura, J. I., Katakuse, M., Calvert, A. T., Sisson, T. W., & Nakai, S. I. (2010). Source materials for inception stage Hawaiian magmas: Pb-He isotope variations for early Kilauea. *Geochemistry, Geophysics, Geosystems*, *11*(3). <https://doi.org/10.1029/2009gc002760>
- Harris, C. R., Millman, K. J., Van Der Walt, S. J., Gommers, R., Virtanen, P., Cournapeau, D., et al. (2020). Array programming with NumPy. *Nature*, *585*(7825), 357–362. <https://doi.org/10.1038/s41586-020-2649-2>
- Harrison, L. N., Weis, D., & Garcia, M. O. (2017). The link between Hawaiian mantle plume composition, magmatic flux, and deep mantle geodynamics. *Earth and Planetary Science Letters*, *463*, 298–309. <https://doi.org/10.1016/j.epsl.2017.01.027>
- Harrison, L. N., Weis, D., & Garcia, M. O. (2020). The multiple depleted mantle components in the Hawaiian-Emperor chain. *Chemical Geology*, *532*, 119324. <https://doi.org/10.1016/j.chemgeo.2019.119324>
- Haskins, E. H., & Garcia, M. O. (2004). Scientific drilling reveals geochemical heterogeneity within the Ko'olau shield, Hawai'i. *Contributions to Mineralogy and Petrology*, *147*(2), 162–188. <https://doi.org/10.1007/s00410-003-0546-y>
- Hauri, E. H. (1996). Major-element variability in the Hawaiian mantle plume. *Nature*, *382*(6590), 415–419. <https://doi.org/10.1038/382415a0>
- Herzberg, C. (2006). Petrology and thermal structure of the Hawaiian plume from Mauna Kea volcano. *Nature*, *444*(7119), 605–609. <https://doi.org/10.1038/nature05254>
- Herzberg, C., Asimow, P. D., Arndt, N., Niu, Y., Leshner, C. M., Fitton, J. G., et al. (2007). Temperatures in ambient mantle and plumes: Constraints from basalts, picrites, and komatiites. *Geochemistry, Geophysics, Geosystems*, *8*(2), Q02006. <https://doi.org/10.1029/2006gc001390>
- Herzberg, C., & Gazel, E. (2009). Petrological evidence for secular cooling in mantle plumes. *Nature*, *458*(7238), 619–622. <https://doi.org/10.1038/nature07857>
- Hieronymus, C. F., & Bercovici, D. (1999). Discrete alternating hotspot islands formed by interaction of magma transport and lithospheric flexure. *Nature*, *397*(6720), 604–607. <https://doi.org/10.1038/17584>
- Hilton, D. R., & Porcelli, D. (2014). Noble gases as tracers of mantle processes. In K. K. Turekian & H. D. Holland (Eds.), *Treatise on geochemistry* (Vol. 3, pp. 327–353). <https://doi.org/10.1016/b978-0-08-095975-7.00206-0>
- Hirschmann, M. M. (2000). Mantle solidus: Experimental constraints and the effects of peridotite composition. *Geochemistry, Geophysics, Geosystems*, *1*(10), 2000GC000070. <https://doi.org/10.1029/2000gc000070>
- Hofmann, A. W. (1997). Mantle geochemistry: The message from oceanic volcanism. *Nature*, *385*(6613), 219–229. <https://doi.org/10.1038/385219a0>
- Hoggard, M. J., Parnell-Turner, R., & White, N. (2020). Hotspots and mantle plumes revisited: Towards reconciling the mantle heat transfer discrepancy. *Earth and Planetary Science Letters*, *542*, 116317. <https://doi.org/10.1016/j.epsl.2020.116317>
- Hounslow, M. W., Domeier, M., & Biggin, A. J. (2018). Subduction flux modulates the geomagnetic polarity reversal rate. *Tectonophysics*, *742*, 34–49. <https://doi.org/10.1016/j.tecto.2018.05.018>
- Huang, S., Abouchami, W., Blichert-Toft, J., Clague, D. A., Cousens, B. L., Frey, F. A., & Humayun, M. (2009). Ancient carbonate sedimentary signature in the Hawaiian plume: Evidence from Mahukona volcano, Hawaii. *Geochemistry, Geophysics, Geosystems*, *10*(8). <https://doi.org/10.1029/2009gc002418>
- Huang, S., & Frey, F. A. (2005). Recycled oceanic crust in the Hawaiian Plume: Evidence from temporal geochemical variations within the Koolau Shield. *Contributions to Mineralogy and Petrology*, *149*(5), 556–575. <https://doi.org/10.1007/s00410-005-0664-9>
- Huang, S., Frey, F. A., Blichert-Toft, J., Fodor, R. V., Bauer, G. R., & Xu, G. (2005). Enriched components in the Hawaiian plume: Evidence from Kahoolawe Volcano, Hawaii. *Geochemistry, Geophysics, Geosystems*, *6*(11), Q11006. <https://doi.org/10.1029/2005gc001012>
- Huang, S., Hall, P. S., & Jackson, M. G. (2011). Geochemical zoning of volcanic chains associated with Pacific hotspots. *Nature Geoscience*, *4*(12), 874–878. <https://doi.org/10.1038/ngeo1263>
- Ishii, T., Kojitani, H., & Akaogi, M. (2019). Phase relations of harzburgite and MORB up to the uppermost lower mantle conditions: Precise comparison with pyrolite by multisample cell high-pressure experiments with implication to dynamics of subducted slabs. *Journal of Geophysical Research: Solid Earth*, *124*(4), 3491–3507. <https://doi.org/10.1029/2018jb016749>
- Ito, G., & Mahoney, J. J. (2005). Flow and melting of a heterogeneous mantle: I. Method and importance to the geochemistry of ocean island and mid-ocean ridge basalts. *Earth and Planetary Science Letters*, *230*(1–2), 29–46. <https://doi.org/10.1016/j.epsl.2004.10.035>
- Jackson, E. D., Shaw, H. R., & Bargar, K. E. (1975). Calculated geochronology and stress field orientations along the Hawaiian chain. *Earth and Planetary Science Letters*, *26*(2), 145–155. [https://doi.org/10.1016/0012-821x\(75\)90082-5](https://doi.org/10.1016/0012-821x(75)90082-5)
- Jackson, M. G., Becker, T. W., & Steinberger, B. (2021). Spatial characteristics of recycled and primordial reservoirs in the deep mantle. *Geochemistry, Geophysics, Geosystems*, *22*(3), e2020GC009525. <https://doi.org/10.1029/2020gc009525>
- Jackson, M. G., Konter, J. G., & Becker, T. W. (2017). Primordial helium entrained by the hottest mantle plumes. *Nature*, *542*(7641), 340–343. <https://doi.org/10.1038/nature21023>
- Jackson, M. G., Weis, D., & Huang, S. (2012). Major element variations in Hawaiian shield lavas: Source features and perspectives from global ocean island basalt (OIB) systematics. *Geochemistry, Geophysics, Geosystems*, *13*(9). <https://doi.org/10.1029/2012gc004268>
- Jones, T. D., Davies, D. R., Campbell, I. H., Iaffaldano, G., Yaxley, G., Kramer, S. C., & Wilson, C. R. (2017). The concurrent emergence and causes of double volcanic hotspot tracks on the Pacific plate. *Nature*, *545*(7655), 472–476. <https://doi.org/10.1038/nature22054>
- King, S. D., & Adam, C. (2014). Hotspot swells revisited. *Physics of the Earth and Planetary Interiors*, *235*, 66–83. <https://doi.org/10.1016/j.pepi.2014.07.006>
- Kumagai, I., Davaille, A., Kurita, K., & Stutzmann, E. (2008). Mantle plumes: Thin, fat, successful, or failing? Constraints to explain hot spot volcanism through time and space. *Geophysical Research Letters*, *35*(16). <https://doi.org/10.1029/2008gl035079>
- Lambart, S., Baker, M. B., & Stolper, E. M. (2016). The role of pyroxenite in basalt genesis: Melt-PX, a melting parameterization for mantle pyroxenites between 0.9 and 5 GPa. *Journal of Geophysical Research: Solid Earth*, *121*(8), 5708–5735. <https://doi.org/10.1002/2015jb012762>
- Lassiter, J. C., & Hauri, E. H. (1998). Osmium-isotope variations in Hawaiian lavas: Evidence for recycled oceanic lithosphere in the Hawaiian plume. *Earth and Planetary Science Letters*, *164*(3–4), 483–496. [https://doi.org/10.1016/s0012-821x\(98\)00240-4](https://doi.org/10.1016/s0012-821x(98)00240-4)
- Le Bars, M., & Davaille, A. (2004). Whole layer convection in a heterogeneous planetary mantle. *Journal of Geophysical Research*, *109*(B3), B03403. <https://doi.org/10.1029/2003jb002617>
- McKinney, W. (2010). Data structures for statistical computing in python. In *Proceedings of the 9th Python in Science Conference* (Vol. 445(1), pp. 51–56).
- Moreira, M. (2013). Noble gas constraints on the origin and evolution of Earth's volatiles. *Geochemical Perspectives*, *2*(2), 229–230. <https://doi.org/10.7185/geochempersp.2.2>
- Morgan, W. J. (1971). Convection plumes in the lower mantle. *Nature*, *230*(5288), 42–43. <https://doi.org/10.1038/230042a0>
- Parai, R. (2025). Noble gases in mantle sources from accretion to the present-day. In *Treatise on geochemistry* (3rd ed., pp. 513–564).
- Parman, S. W. (2007). Helium isotopic evidence for episodic mantle melting and crustal growth. *Nature*, *446*(7138), 900–903. <https://doi.org/10.1038/nature05691>

- Pertermann, M., Hirschmann, M. M., Hametner, K., Günther, D., & Schmidt, M. W. (2004). Experimental determination of trace element partitioning between garnet and silica-rich liquid during anhydrous partial melting of MORB-like eclogite. *Geochemistry, Geophysics, Geosystems*, 5, Q05a01. <https://doi.org/10.1029/2003gc000638>
- Pin, C., Briot, D., Bassin, C., & Poitrasson, F. (1994). Concomitant separation of strontium and samarium-neodymium for isotopic analysis in silicate samples, based on specific extraction chromatography. *Analytica Chimica Acta*, 298(2), 209–217. [https://doi.org/10.1016/0003-2670\(94\)00274-6](https://doi.org/10.1016/0003-2670(94)00274-6)
- Plank, T., & Langmuir, C. H. (1998). The chemical composition of subducting sediment and its consequences for the crust and mantle. *Chemical Geology*, 145(3–4), 325–394. [https://doi.org/10.1016/s0009-2541\(97\)00150-2](https://doi.org/10.1016/s0009-2541(97)00150-2)
- Putirka, K. D. (2005). Mantle potential temperatures at Hawaii, Iceland, and the mid-ocean ridge system, as inferred from olivine phenocrysts: Evidence for thermally driven mantle plumes. *Geochemistry, Geophysics, Geosystems*, 6(5). <https://doi.org/10.1029/2005gc000915>
- Putirka, K. D. (2008). Thermometers and barometers for volcanic systems. *Reviews in Mineralogy and Geochemistry*, 69(1), 61–120. <https://doi.org/10.2138/rmg.2008.69.3>
- Ren, Z. Y., Hanyu, T., Miyazaki, T., Chang, Q., Kawabata, H., Takahashi, T., et al. (2009). Geochemical differences of the Hawaiian shield lavas: Implications for melting process in the heterogeneous Hawaiian plume. *Journal of Petrology*, 50(8), 1553–1573. <https://doi.org/10.1093/ptrology/egp041>
- Rhodes, J. M., & Vollinger, M. J. (2004). Composition of basaltic lavas sampled by phase-2 of the Hawaii Scientific Drilling Project: Geochemical stratigraphy and magma types. *Geochemistry, Geophysics, Geosystems*, 5(3). <https://doi.org/10.1029/2002gc000434>
- Ribe, N., Davaille, A., & Christensen, U. (2007). Fluid dynamics of mantle plumes. In *Mantle plumes* (pp. 1–48). Springer.
- Ricolleau, A., Perrillat, J. P., Fiquet, G., Daniel, I., Matas, J., Addad, A., et al. (2010). Phase relations and equation of state of a natural MORB: Implications for the density profile of subducted oceanic crust in the Earth's lower mantle. *Journal of Geophysical Research*, 115(B8), B08202. <https://doi.org/10.1029/2009jb006709>
- Ringwood, A. E. (1969). *Composition and evolution of the upper mantle* (Vol. 13, pp. 1–17). American Geophysical Union Geophysical Monograph Series. <https://doi.org/10.1029/gm013p0001>
- Robinson, J. A. C., & Wood, B. J. (1998). The depth of the spinel to garnet transition at the peridotite solidus. *Earth and Planetary Science Letters*, 164(1–2), 277–284. [https://doi.org/10.1016/s0012-821x\(98\)00213-1](https://doi.org/10.1016/s0012-821x(98)00213-1)
- Rudnick, R. L., & Gao, S. (2003). Composition of the continental crust. In R. L. Rudnick (Ed.), *The Crust* (Vol. 3, pp. 1–64).
- Salters, V. J., Blichert-Toft, J., Fekiacova, Z., Sachi-Kocher, A., & Bizimis, M. (2006). Isotope and trace element evidence for depleted lithosphere in the source of enriched Ko'olau basalts. *Contributions to Mineralogy and Petrology*, 151(3), 297–312. <https://doi.org/10.1007/s00410-005-0059-y>
- Salters, V. J., Mallick, S., Hart, S. R., Langmuir, C. E., & Stracke, A. (2011). Domains of depleted mantle: New evidence from hafnium and neodymium isotopes. *Geochemistry, Geophysics, Geosystems*, 12(8), Q08001. <https://doi.org/10.1029/2011gc003617>
- Salters, V. J., & Stracke, A. (2004). Composition of the depleted mantle. *Geochemistry, Geophysics, Geosystems*, 5(5), Q05004. <https://doi.org/10.1029/2003gc000597>
- Sanfilippo, A., Stracke, A., Genske, F., Scarani, S., Cuffaro, M., Basch, V., et al. (2024). Upwelling of melt-depleted mantle under Iceland. *Nature Geoscience*, 17(10), 1–7. <https://doi.org/10.1038/s41561-024-01532-z>
- Sani, C., Sanfilippo, A., Ferrando, C., Peyve, A. A., Skolotnev, S. G., Muccini, F., et al. (2020). Ultra-depleted melt refertilization of mantle peridotites in a large intra-transform domain (Doldrums Fracture Zone; 7–8° N, Mid Atlantic Ridge). *Lithos*, 374, 105698. <https://doi.org/10.1016/j.lithos.2020.105698>
- Sarbas, B. (2008). The GEOROC database as part of a growing geoinformatics network. In *Geoinformatics 2008—data to knowledge* (pp. 42–43). USGS.
- Shuttle, O., MacLennan, J., & Lambart, S. (2014). Quantifying lithological variability in the mantle. *Earth and Planetary Science Letters*, 395, 24–40. <https://doi.org/10.1016/j.epsl.2014.03.040>
- Simmons, N. A., Forte, A. M., Boschi, L., & Grand, S. P. (2010). GyPSuM: A joint tomographic model of mantle density and seismic wave speeds. *Journal of Geophysical Research*, 115(B12). <https://doi.org/10.1029/2010jb007631>
- Sobolev, A. V., Hofmann, A. W., Kuzmin, D. V., Yaxley, G. M., Arndt, N. T., Chung, S. L., et al. (2007). The amount of recycled crust in sources of mantle-derived melts. *Science*, 316(5823), 412–417. <https://doi.org/10.1126/science.1138113>
- Sobolev, A. V., Hofmann, A. W., Sobolev, S. V., & Nikogosian, I. K. (2005). An olivine-free mantle source of Hawaiian shield basalts. *Nature*, 434(7033), 590–597. <https://doi.org/10.1038/nature03411>
- Stracke, A. (2012). Earth's heterogeneous mantle: A product of convection-driven interaction between crust and mantle. *Chemical Geology*, 330, 274–299. <https://doi.org/10.1016/j.chemgeo.2012.08.007>
- Stracke, A. (2025). The geochemical concept of a “Primitive Mantle”. In *Treatise on geochemistry* (3rd ed., pp. 1–16).
- Stracke, A., & Béguélin, P. (2024). Basalts record a limited extent of mantle depletion: Cause and chemical geodynamic implications. *Geochemical Perspectives Letters*, 32, 21–26. <https://doi.org/10.7185/geochemlet.2437>
- Stracke, A., Bizimis, M., & Salters, V. J. (2003). Recycling oceanic crust: Quantitative constraints. *Geochemistry, Geophysics, Geosystems*, 4(3), 8003. <https://doi.org/10.1029/2001GC000223>
- Stracke, A., & Bourdon, B. (2009). The importance of melt extraction for tracing mantle heterogeneity. *Geochimica et Cosmochimica Acta*, 73(1), 218–238. <https://doi.org/10.1016/j.gca.2008.10.015>
- Stracke, A., Genske, F., Berndt, J., & Koornneef, J. M. (2019). Ubiquitous ultra-depleted domains in Earth's mantle. *Nature Geoscience*, 12(10), 851–855. <https://doi.org/10.1038/s41561-019-0446-z>
- Stracke, A., Salters, V. J., & Sims, K. W. (1999). Assessing the presence of garnet-pyroxenite in the mantle sources of basalts through combined hafnium-neodymium-thorium isotope systematics. *Geochemistry, Geophysics, Geosystems*, 1(12), 1006. <https://doi.org/10.1029/1999GC000013>
- Stracke, A., Willig, M., Genske, F., Béguélin, P., & Todd, E. (2022). Chemical geodynamics insights from a machine learning approach. *Geochemistry, Geophysics, Geosystems*, 23(10), e2022GC010606. <https://doi.org/10.1029/2022gc010606>
- Tackley, P. J. (2011). Living dead slabs in 3-D: The dynamics of compositionally-stratified slabs entering a “slab graveyard” above the core-mantle boundary. *Physics of the Earth and Planetary Interiors*, 188(3–4), 150–162. <https://doi.org/10.1016/j.pepi.2011.04.013>
- Tanaka, R., & Nakamura, E. (2005). Boron isotopic constraints on the source of Hawaiian shield lavas. *Geochimica et Cosmochimica Acta*, 69(13), 3385–3399. <https://doi.org/10.1016/j.gca.2005.03.009>
- Tanaka, R., Nakamura, E., & Takahashi, E. (2002). Geochemical evolution of Koolau volcano, Hawaii. *GEOPHYSICAL MONOGRAPH-AMERICAN GEOPHYSICAL UNION*, 128, 311–332. <https://doi.org/10.1029/gm128p0311>
- Tatsumoto, M. (1978). Isotopic composition of lead in oceanic basalt and its implication to mantle evolution. *Earth and Planetary Science Letters*, 38(1), 63–87. [https://doi.org/10.1016/0012-821x\(78\)90126-7](https://doi.org/10.1016/0012-821x(78)90126-7)

- Tauzin, B., Waszek, L., Ballmer, M. D., Afonso, J. C., & Bodin, T. (2022). Basaltic reservoirs in the Earth's mantle transition zone. *Proceedings of the National Academy of Sciences*, *119*(48), e2209399119. <https://doi.org/10.1073/pnas.2209399119>
- Tazoe, H., Obata, H., Amakawa, H., Nozaki, Y., & Gamo, T. (2007). Precise determination of the cerium isotopic compositions of surface seawater in the Northwest Pacific Ocean and Tokyo Bay. *Marine Chemistry*, *103*(1–2), 1–14. <https://doi.org/10.1016/j.marchem.2006.05.008>
- Tazoe, H., Obata, H., & Gamo, T. (2007). Determination of cerium isotope ratios in geochemical samples using oxidative extraction technique with chelating resin. *Journal of Analytical Atomic Spectrometry*, *22*(6), 616–622. <https://doi.org/10.1039/b617285g>
- Tucker, J. M., van Keken, P. E., & Ballentine, C. J. (2022). Earth's missing argon paradox resolved by recycling of oceanic crust. *Nature Geoscience*, *15*(1), 85–90. <https://doi.org/10.1038/s41561-021-00870-6>
- Van Ark, E., & Lin, J. (2004). Time variation in igneous volume flux of the Hawaii-Emperor hot spot seamount chain. *Journal of Geophysical Research*, *109*(B11), B11401. <https://doi.org/10.1029/2003JB002949>
- Vidal, V., & Bonneville, A. (2004). Variations of the Hawaiian hot spot activity revealed by variations in the magma production rate. *Journal of Geophysical Research*, *109*(B3), B03104. <https://doi.org/10.1029/2003jb002559>
- Virtanen, P., Gommers, R., Oliphant, T. E., Haberland, M., Reddy, T., Cournapeau, D., et al. (2020). SciPy 1.0: Fundamental algorithms for scientific computing in Python. *Nature Methods*, *17*(3), 261–272. <https://doi.org/10.1038/s41592-019-0686-2>
- Walter, M., & Cottrell, E. (2025). Equilibrium constraints on partial melting in the upper mantle. In *Treatise on geochemistry* (3rd ed., pp. 231–273).
- Weis, D., Garcia, M. O., Rhodes, J. M., Jellinek, M., & Scoates, J. S. (2011). Role of the deep mantle in generating the compositional asymmetry of the Hawaiian mantle plume. *Nature Geoscience*, *4*(12), 831–838. <https://doi.org/10.1038/ngeo1328>
- Weis, D., Harrison, L. N., McMillan, R., & Williamson, N. M. (2020). Fine-scale structure of Earth's deep mantle resolved through statistical analysis of Hawaiian basalt geochemistry. *Geochemistry, Geophysics, Geosystems*, *21*(11), e2020GC009292. <https://doi.org/10.1029/2020gc009292>
- Weis, D., Kieffer, B., Maerschalk, C., Pretorius, W., & Barling, J. (2005). High-precision Pb-Sr-Nd-Hf isotopic characterization of USGS BHVO-1 and BHVO-2 reference materials. *Geochemistry, Geophysics, Geosystems*, *6*(2). <https://doi.org/10.1029/2004gc000852>
- Wessel, P. (2016). Regional–residual separation of bathymetry and revised estimates of Hawaii plume flux. *Geophysical Journal International*, *204*(2), 932–947. <https://doi.org/10.1093/gji/ggv472>
- White, W. M. (2010). Oceanic island basalts and mantle plumes: The geochemical perspective. *Annual Review of Earth and Planetary Sciences*, *38*(1), 133–160. <https://doi.org/10.1146/annurev-earth-040809-152450>
- Willig, M., & Stracke, A. (2018). Accurate and precise measurement of Ce isotope ratios by thermal ionization mass spectrometry (TIMS). *Chemical Geology*, *476*, 119–129. <https://doi.org/10.1016/j.chemgeo.2017.11.010>
- Willig, M., & Stracke, A. (2019). Earth's chondritic light rare earth element composition: Evidence from the Ce–Nd isotope systematics of chondrites and oceanic basalts. *Earth and Planetary Science Letters*, *509*, 55–65. <https://doi.org/10.1016/j.epsl.2018.12.004>
- Willig, M., Stracke, A., Beier, C., & Salters, V. J. (2020). Constraints on mantle evolution from Ce–Nd–Hf isotope systematics. *Geochimica et Cosmochimica Acta*, *272*, 36–53. <https://doi.org/10.1016/j.gca.2019.12.029>
- Xu, G., Frey, F. A., Clague, D. A., Abouchami, W., Blichert-Toft, J., Cousens, B., & Weisler, M. (2007). Geochemical characteristics of West Molokai shield-and postshield-stage lavas: Constraints on Hawaiian plume models. *Geochemistry, Geophysics, Geosystems*, *8*(8). <https://doi.org/10.1029/2006gc001554>
- Xu, G., Huang, S., Frey, F. A., Blichert-Toft, J., Abouchami, W., Clague, D. A., et al. (2014). The distribution of geochemical heterogeneities in the source of Hawaiian shield lavas as revealed by a transect across the strike of the Loa and Kea spatial trends: East Molokai to West Molokai to Penguin Bank. *Geochimica et Cosmochimica Acta*, *132*, 214–237. <https://doi.org/10.1016/j.gca.2014.02.002>
- Yamasaki, S., Kani, T., Hanan, B. B., & Tagami, T. (2009). Isotopic geochemistry of Hualalai shield-stage tholeiitic basalts from submarine North Kona region, Hawaii. *Journal of Volcanology and Geothermal Research*, *185*(3), 223–230. <https://doi.org/10.1016/j.jvolgeores.2009.06.006>